Selective Activation of Aromatic C-H Bonds Catalyzed by Single Gold Atoms at Room Temperature

Benjamin Lowe,[†,‡,⊥] Jack Hellerstedt,[†,‡,⊥] Adam Matěj,[¶,§,‖,⊥] Pingo Mutombo,[¶] Dhaneesh Kumar,[†,‡] Martin Ondráček,[¶] Pavel Jelinek,[*,¶,§] and Agustin Schiffrin[*,†,‡]

†*School of Physics and Astronomy, Monash University, Clayton, Victoria 3800, Australia*

‡*ARC Centre for Excellence in Low-Energy Electronics Technologies, Monash University, Clayton, Victoria 3800, Australia*

¶*Institute of Physics, Academy of Sciences of the Czech Republic, Cukrovarnická 10, 1862 53, Prague, Czech Republic*

§*Regional Centre of Advanced Technologies and Materials, Czech Advanced Technology and Research Institute (CATRIN), Palacký University Olomouc, 779 00 Olomouc, Czech Republic*

‖*Department of Physical Chemistry, Faculty of Science, Palacký University Olomouc, 771 46 Olomouc, Czech Republic*

⊥*Contributed equally to this work*

E-mail: jelinekp@fzu.cz; agustin.schiffrin@monash.edu

Abstract

Selective activation and controlled functionalization of C-H bonds in organic molecules is one of the most desirable processes in synthetic chemistry. Despite progress in het-

1

erogeneous catalysis using metal surfaces, this goal remains challenging due to the stability of C-H bonds and their ubiquity in precursor molecules, hampering regioselectivity. Here, we examine the interaction between 9,10-dicyanoanthracene (DCA) molecules and Au adatoms on an Ag(111) surface at room temperature (RT). Characterization via low-temperature scanning tunneling microscopy, spectroscopy, and non-contact atomic force microscopy, supported by theoretical calculations, revealed the formation of organometallic DCA-Au-DCA dimers, where C atoms at the ends of the anthracene moieties are bonded covalently to single Au atoms. The formation of this organometallic compound is initiated by a regioselective cleaving of C-H bonds at RT. Hybrid quantum mechanics/molecular mechanics calculations show that this regioselective C-H bond cleaving is enabled by an intermediate metal-organic complex which significantly reduces the dissociation barrier of a specific C-H bond. Harnessing the catalytic activity of single metal atoms, this regioselective on-surface C-H activation reaction at RT offers promising routes for future synthesis of functional organic and organometallic materials.

Introduction

The selective activation and controlled functionalization of C-H bonds in molecular precursors is one of the most important areas of synthetic organic chemistry for the design of C-C and C-heteroatom bonds in new compounds.[1–3] Controlled C-H activation reactions have enticing applications including natural gas transport,[2,4,5] polymer fabrication,[6–8] and late-stage modification of pharmaceutical products.[9–14] The high bond-dissociation enthalpy and ubiquity of C-H bonds, however, make their selective cleavage challenging.[1,15–17] In solution, enzymatic and transition metal (homogeneous) catalysis have provided avenues for the selective activation of C-H bonds.[7,18–21]

Solid metal surfaces have also been shown to exhibit (heterogeneous) catalytic activity on adsorbed molecules.[22–25] In particular, controlled activation of aromatic C-H bonds on a

surface has enabled the synthesis of low-dimensional organic nanomaterials with promising electronic and magnetic properties, such as nanographenes,[26–29] graphene nanoribbons,[30–32] organic polymers,[33,34] and covalent organic frameworks.[35,36] However, broader application of on-surface C-H activation for the synthesis of functional materials remains limited due to high-bond energies and poor regioselectivity.[37,38]

A common reaction used for on-surface design of aromatic C-C and C-heteroatom bonds is Ullmann-type coupling, where C-X bonds (X: halogen atom) in precursor molecules undergo surface-catalyzed dehalogenation.[39] This approach has been successfully exploited for the fabrication of a range of different materials,[22–25,39] although the requirement for pre-halogenation of targeted carbons in precursor molecules limits its applicability.

One promising approach for on-surface aromatic C-H activation consists of leveraging the catalytic activity of single metal adatoms. Single-atom catalysis yields promise for reducing the amount of precious metals used in heterogeneous catalysis.[40–43] In particular, despite its relative chemical inertness, gold has emerged as a promising single-atom catalyst (e.g., for the oxidation of carbon monoxide).[42–44] While Au surfaces have been used to catalyze the cleavage of C-H and C-X bonds,[38,45–47] sometimes resulting in the formation of organometallic C-Au bonds,[48–50] atomic-scale studies of single Au atom catalysis for C-H activation (on surfaces other than Au) have not yet been conducted.

Herein, we report the regioselective cleavage of an aromatic C-H bond of a cyano-functionalized anthracene derivative, 9,10-dicyanoanthracene (DCA; Figure 1a), activated by the interaction with single Au atoms on a Ag(111) surface at room temperature (RT). This selective activation of a specific C-H bond (located at the end of the anthracene group - labelled position A in Figure 1a) is mediated by the on-surface formation of an intermediate DCA-Au metal-organic complex, which subsequently enables selective dehydrogenation of the DCA molecule (Figure 1d). This results in a reactive site at the DCA anthracene extremity, which can then covalently bond to a Au adatom and form organometallic DCA-Au-DCA dimers via a C-Au-C motif (Figure 1e). We used low-temperature scanning tunneling

microscopy (STM) and spectroscopy (STS) as well as non-contact atomic force microscopy (ncAFM) to characterize the organometallic dimers at the atomic scale. The experimental findings are supported by density functional theory (DFT), ncAFM simulations and quantum mechanics/molecular mechanics (QM/MM) calculations to shed light on the atomic structure and reaction mechanism. The low activation energy, indicated by the reaction occurring at RT, and regioselectivity of the observed C-H activation open the door to unexplored on-surface synthesis protocols based on single atom catalysis for the development of functional and robust organic and organometallic materials.

Results

We co-deposited DCA molecules and Au atoms from the gas phase in ultra-high vacuum (UHV) onto a clean Ag(111) surface held at RT (see Methods for further details). Figure 1f shows an STM image of a sample region following this preparation. We observe two types of well-ordered, two-dimensional (2D) periodic arrays of self-assembled adsorbates: (i) a purely organic domain (cyan box, region labelled DCA) consisting of identical elliptical protrusions (solid blue outline) corresponding to non-covalently bonded DCA molecules;[51] (ii) a domain consisting of parallel rows of pairs (red box, region labelled DCA+Au) of similar elliptical features (inset: solid blue outline) linked by circular protrusions (inset: red dashed circular outline). Based on their appearance and size, we identify the elliptical features in the DCA+Au domain as DCA molecules,[51] arranged in pairs in either cis (red box in Figure 1f) or trans configuration (see SI Figure S1). Approximately equal occurrences of cis- and trans- configuration were observed, though a quantitative statistical analysis is beyond the scope of this study.

The qualitative difference in Figure 1f between the previously reported[51] DCA domain and the DCA+Au domain consisting of ordered DCA pairs is a strong suggestion that the pairing of DCA molecules in the latter is mediated by the interaction between DCA and

Au adatoms. Notably, these results are also qualitatively different from previously studied surface-supported systems where 3-fold rotationally symmetric metal-ligand coordination between DCA cyano groups and noble metal adatoms [e.g., Cu adatoms on Cu(111),[52–54] Ag(111),[55] Ir(111)-supported graphene,[56] and NbSe$_2$;[57] Au adatoms on Au(111)[58]] give rise to porous, 2D honeycomb-kagome metal-organic frameworks (MOFs) as shown in Figure 1b. This is a strong indication that the interaction between DCA and Au adatoms on Ag(111) is fundamentally different than in these other systems.

We used ncAFM with a carbon-monoxide (CO)-functionalized tip (see Methods) to gain further insight into the intramolecular structure of the Au-mediated DCA pairs. NcAFM imaging of the DCA+Au domain, Figure 1g, and the DCA domain,[51] Figure 1h, are similar in that the submolecular structure of individual DCA molecules is clearly resolved in agreement with the overlaid chemical structure in Figure 1h, with non-covalent attractive N--H interactions (Figure 1 white arrows) between adjacent molecules (DCA) or molecule pairs (DCA+Au).[59]

In contrast with ncAFM imaging of the DCA domain in Figure 1h where the frequency shift (Δf) across each of the DCA benzene rings is relatively uniform, individual DCA molecules in the DCA+Au domain, Figure 1g, exhibit reduced Δf at the benzene rings closest to the DCA pair center (near the location of the circular protrusion in STM imaging; red dashed circle). Such ncAFM appearance of π-conjugated rings is indicative of direct coordination between atoms of the aromatic group and a metal adatom,[60–63] further supporting the involvement of Au adatoms within the DCA+Au domain.

We conducted lateral STM manipulation to further probe the nature of the intra- and inter-DCA pair interactions within the DCA+Au assembly. Figure 2a shows an STM image of a DCA+Au domain with cis-configuration DCA pairs. Individual DCA pairs, consisting of two elliptical features connected via a circular feature in STM images, could be reproducibly removed from the edge of a DCA+Au domain and manipulated about the surface (Figure 2b-d). Upon manipulation, the STM appearance of the DCA pairs is unchanged, suggesting

that their chemical structure is preserved.

In some instances, we observed switching from the cis- to the trans- configuration upon manipulation (dashed green and purple pairs in Figure 2). We did not, however, observe evidence of such switching under normal tunneling conditions (through e.g. telegraph noise[64]); cis- and trans- configurations were both otherwise stable during characterization.

Within the range of STM manipulation parameters tested, we were unable to observe further breaking of the DCA pairs into their individual constituents (i.e. STM elliptical features corresponding to DCA molecules and circular features). From this, we conclude that while lateral manipulation can overcome the strength of bonding between adjacent DCA pairs, it cannot overcome the interaction connecting the two DCA molecules within such pairs. This suggests the intra-pair interaction is significantly stronger than the inter-pair interaction, and that the Au-mediated DCA pairs are highly stable.

From these STM manipulation observations, combined with the reduced frequency shift of the benzene rings near the DCA pair center (Figure 1f, 3c), we propose that the DCA pairs consist of an organometallic DCA-Au-DCA motif, wherein a position A (Figure 1a) carbon atom of each of the two DCA molecules is covalently bonded to a Au atom (Figure 1e). The observation of cis- and trans- configurations can be attributed to the chemical equivalence of the two carbon atoms at the anthracene ends of the DCA molecule.

We performed DFT calculations to rationalize the proposed organometallic structure. The energetically favorable atomic structure of an organometallic trans DCA-Au-DCA dimer on Ag(111), optimized via DFT (see Methods), is shown in Figure 3a). The DFT calculations revealed a negligible energy difference between the trans and cis configurations (see SI Figure S2), supporting the observation of the two configurations in approximately equal measure, and the cis-to-trans conversion by STM manipulation.

The simulated ncAFM image (Figure 3b; obtained via the probe-particle method[65]) corresponding to the DFT-relaxed DCA-Au-DCA dimer in Figure 3a shows strong qualitative agreement with the experimental ncAFM image (Figure 3c), including the reduced Δf of the

benzene rings closest to the C-Au-C bonding motif at the DCA pair center. The simulated and experimental image also have a similar distance d between the centers of the benzene rings closest to the Au atom (5.72 ± 0.06 Å for the simulated images and 6.0 ± 0.2 Å for the experimental images). We rule out a DCA-DCA pair with a direct covalent C-C bond between facing anthracene groups, since ncAFM simulations of this structure would result in a distance d (4.76 ± 0.06 Å) significantly shorter than that observed experimentally, and would not reproduce the experimentally observed reduced Δf in the benzene rings closest to the DCA-DCA linkage (Figure S3).

We performed dI/dV STS to gain insight into the electronic structure of an individual DCA-Au-DCA dimer. The spectra in Figure 4a were acquired on the Au (orange) and outer (i.e. furthest from Au site) anthracene end (blue) sites of a trans DCA-Au-DCA dimer, removed from the 2D assembly via manipulation. Both orange and blue spectra show a step-like feature at ∼-66 mV, and a peak at ∼376 and ∼560 mV, respectively.

We attribute the step-like feature to the Shockley surface state of Ag(111),[66] and the two peaks to intrinsic electronic states of the DCA-Au-DCA unit. Figure 4b,c show dI/dV maps associated with each of these electronic states. Both maps show significant intensity at the anthracene ends furthest from the Au site, and at the cyano groups. These features are qualitatively similar to the spatial distribution of the DCA lowest unoccupied molecular orbital (LUMO).[51,67] The map in Figure 4b also shows some dI/dV intensity at the Au site, significantly more so than Figure 4c (emphasized in the difference between Figure 4b and Figure 4c, displayed in Figure 4d).

Figure 4e,f shows the DFT-calculated spatial distribution of the LUMO and LUMO+1 of the structurally optimized gas-phase DCA-Au-DCA dimer (see Methods and Figure S4 in the SI). These DFT-calculated LUMO and LUMO+1 are separated in energy by ∼100 meV, on the same order of magnitude as the ∼184 meV energy difference between experimental dI/dV peaks in Figure 4a. Both the calculated LUMO and LUMO+1 have predominantly DCA orbital character (see Figure S4 and Figure S5), with intensity at the anthracene

ends furthest from the Au site, and at the cyano groups. The LUMO (Figure 4e) shows intensity at the Au atom whereas the LUMO+1 (Figure 4f) exhibits a nodal plane at this site perpendicular to the DCA-DCA axis. The calculated LUMO and LUMO+1 are in qualitative agreement with the experimental dI/dV maps in Figure 4b and c, respectively. This agreement provides further evidence that the DCA+Au self-assembled 2D domain in Figure 1f) consists of organometallic DCA-Au-DCA dimers, in which the position A carbon atoms are covalently bonded to a Au atom.

The organometallic DCA-Au-DCA structure is qualitatively different to previously observed 2D MOFs consisting of DCA molecules coordinated with metal atoms via their cyano groups.[52–58] Moreover, the formation of the organometallic DCA-Au-DCA motif requires highly regioselective cleavage of the position A aromatic C-H bonds to enable the C-Au-C covalent bonding. Such C-H bonds have large dissociation enthalpies,[60,68,69] ΔH, meaning their cleavage seldom occurs at RT,[70] and they often suffer from poor regioselectivity.[25,38,60,68,69] For a gas-phase DCA molecule for instance, we calculated ΔH values of 112.1 and 113.2 kcal/mol (4.86 and 4.91 eV) via DFT for the aromatic C-H bonds at positions A and B, respectively (see Figure 1a and SI Figure S7).

In the following, we rationalize the highly selective C-H activation reaction (and subsequent DCA-Au-DCA formation) at RT via DFT and QM/MM calculations. First, we found using DFT that Au adatoms on Ag(111) retain their neutral, atomic-like character (SI Figure S6). This contrasts with the case of Au adatoms on Au(111), where significant electronic hybridization between adatom and the surface takes place. That is, Au adatoms are less coordinated and arguably more reactive on Ag(111) than on Au(111), providing an explanation for the differences between organometallic (covalent C-Au bonding) and metal-organic[58] (N--Au) coordination complexes (Figure 1).

We then conducted QM/MM calculations of Gibbs free energy differences, ΔG, on a system composed of a single DCA molecule with a single Au adatom in proximity on Ag(111) (system 1; see Figures 5b and S7). We considered a C-H bond dissociation mechanism

mediated by the direct interaction between Au and H at $T = 300$ K ($\sim$RT to match our experimental conditions; see Figures S7 and S8 for calculations at $T = 0$ K). The dashed blue curve in Figure 5a) shows the calculated ΔG as a function of position A C-H distance, $d_{\text{C-H}}$, when system 1 evolves from an initial state $\text{IS}_{1\text{A}}$ to a transition state $\text{TS}_{1\text{A}}$ then to an intermediate state $\text{IM}_{1\text{A}}$ (where H becomes bonded to Au; Figure 5b). These calculations yielded an activation energy $\Delta G\,[\text{IS}_{1\text{A}} \rightarrow \text{TS}_{1\text{A}}] = 27.7$ kcal/mol (1.20 eV). We claim that this energy is too high to explain the dissociation of an anthracene C-H bond at RT. Note that similar calculations performed for the position B C-H bond in system 1 suggest an even higher dissociation barrier (Figure S7).

Therefore, we also considered a system composed of two DCA molecules and a single Au adatom on Ag(111) (system 2; Figures 5c and S8), with a configuration similar to that at the edges of self-assembled DCA-only domains (Figures 1a and S14).[51] We suggest that Au atoms diffusing on the surface may encounter supramolecular DCA islands rather than isolated molecules (Figure S14 and S15). This is supported by the fact that, experimentally, we observed DCA-Au-DCA dimers both when DCA and Au were deposited sequentially (DCA first) or simultaneously (see Methods). Furthermore, we did not observe any DCA+Au domains which were surrounded by DCA-only domains. Based on this, we considered the possibility that N--Au coordination could give rise to a metal-organic DCA(N)--Au complex (see initial states $\text{IS}_{2\text{A}}$ or $\text{IS}_{2\text{B}}$ in Figure 5c,d) at the edges of DCA-only domains, and conducted QM/MM simulations to investigate whether this geometry could facilitate C-H activation at an adjacent molecule. The solid blue curve in Figure 5a) shows $\Delta G(T = 300$ K) as a function of position A C-H distance, $d_{\text{C-H}}$, for system 2 as it evolves from $\text{IS}_{2\text{A}}$ to an intermediate state $\text{IM}_{2\text{A}}$ via a transition state $\text{TS}_{2\text{A}}$ (Figure 5c). Here, we found a position A C-H activation energy $\Delta G\,[\text{IS}_{2\text{A}} \rightarrow \text{TS}_{2\text{A}}] = 19.1$ kcal/mol (0.83 eV), significantly smaller than $\Delta G\,[\text{IS}_{1\text{A}} \rightarrow \text{TS}_{1\text{A}}]$.

Similarly, the red curve in Figure 5a) corresponds to $\Delta G(T = 300$ K) as a function of $d_{\text{C-H}} - d_{\text{Au-H}}$ for the position B C-H bond, for the same system 2, evolving from $\text{IS}_{2\text{B}}$ to

TS_{2B} to IM_{2B} (Figure 5d). Here, the activation barrier $\Delta G\,[IS_{2B} \rightarrow TS_{2B}]$ for the position B C-H bond is 33.6 kcal/mol (1.46 eV), significantly larger than $\Delta G\,[IS_{2A} \rightarrow TS_{2A}]$. Based on these QM/MM calculations, the dissociation barrier of the position A C-H bonds is significantly lowered via interaction with a DCA(N)--Au metal-organic complex, enabling highly regioselective C-H bond cleavage at RT.

Discussion

To gain more insight into the regioselective lowering of the activation energy of the C-H cleavage, we analyzed the electronic structure of the DCA(N)--Au complex (present in IS_{2A}) using DFT (Figure S10b). These calculations indicate a weak, purely electrostatic interaction between Au and cyano group, with no evidence of strong hybridization, and with an interaction energy of 4.2 kcal/mol (0.18 eV) and a N--Au distance of 2.47 Å. This interaction with the cyano group results in a local polarization around and charge redistribution within the Au atom, with an electron depletion on the outside of the Au atom along the Au-cyano axis (Figure S10d). This depleted electron density can reduce the Pauli repulsion between Au and a H atom of an adjacent DCA, facilitating the formation of a Au-H chemical bond and of a DCA(H)-Au--(N)DCA complex (see IM_{2A} in Figure 5c). This partially explains the significant lowering of the C-H bond activation energy.

Our DFT calculations also show that, in IM_{2A} (Figure 5), covalent Au-H bonding is concomitant with hybridization of Au 6s and 5d orbitals, giving rise to two hybrid sd orbitals along the N--Au-H axis (see SI Section S9, Figures S9-S13), and with electron transfer from Au to H (Figure S12). The resulting partial positive charge on Au strengthens the electrostatic interaction with the partially negatively charged cyano group (Figure S11), causing an increase in the Au--(N)DCA interaction energy of ∼22 kcal/mol (∼0.95 eV) and a reduction of the Au--N bond length by ∼0.27 Å.

To understand how this change in Au--(N)DCA interaction energy influences the C-

H cleavage activation barrier, it is pertinent to consider the transition state TS_{2A} (Figure 5). Here, DFT calculations show a Au--(N)DCA interaction energy of 26.0 kcal/mol (1.13 eV) with a Au--N bond length of 2.17 Å - indicating a much stronger interaction than in IS_{2A}. This synergistic effect therefore contributes further to the significant lowering of the activation energy of the C-H cleavage at position A.

Moreover, we claim that, for the position B C-H bond (Figure 5d), this effect is offset by steric hindrance and N-N repulsion between adjacent DCA molecules, contributing to a significantly larger dissociation barrier $\Delta G\,[IS_{2B} \rightarrow TS_{2B}]$.

For TS_{2A}, we calculated via DFT a C-H stretching mode in the direction of the C-H dissociation with an eigenfrequency of 611.5 cm^{-1}. Using this value, we calculated for position A (with a dissociation barrier of 19 kcal/mol) at RT an Arrhenius[71] C-H dissociation rate constant of 0.23 s^{-1}. By contrast, the RT Arrhenius dissociation rate constant for the position B C-H bond (with a dissociation barrier of 33.6 kcal/mol) is 1.4×10^{-12} s^{-1}. We claim that this significant difference between positions A and B explains the experimentally observed regioselectivity of the C-H dissociation. The 19 kcal/mol barrier represents a significant reduction relative to comparable C-H activation reactions with barriers of 30-40 kcal/mol (1.3-1.8 eV), experimentally occurring in a temperature window of 400-700 K.[60,68,69,72] Furthermore, other on-surface reactions with barriers of ~20 kcal/mol (~0.87 eV) have been observed at RT,[71,73] supporting the interpretation of our experimental results as RT C-H activation.

Although our DFT and QM/MM calculations rationalize the regioselective cleaving of position A C-H bonds at RT, they do not explain the pathway from IM_{2A} (Figure 5) to the experimentally observed organometallic DCA-Au-DCA motif (where C bonds covalently to Au). In the following, we provide a tentative, qualitative scenario for such a pathway. We propose that, at RT, the hydrogen atom in DCA(N)--Au-H in IM_{2A} (Figure 5c) is likely to detach, bind to Ag(111) and then desorb (see SI Section S10), leaving organometallic DCA(C)-Au on Ag(111) which can diffuse on the surface and potentially react with an-

other dehydrogenated DCA· radical, forming the experimentally observed DCA-Au-DCA unit. Non-covalent N--H bonds between neighboring DCA-Au-DCA dimers may contribute to stabilizing the DCA-Au-DCA dimer rows as seen in the DCA-Au domain in Figure 1f. The relatively weak and reversible DCA(N)--Au interaction, combined with the reactivity of the DCA· radical, might explain why we did not experimentally observe any of the metal-organic DCA(N)--Au species such as in IS_{2A} or IM_{2A} in Figure 5. A quantitative theoretical description of this process would require the consideration of many possible reaction pathways (including, for example, surface diffusion, dynamic equilibrium of different phases) in a system composed of many DCA molecules, Au adatoms and DCA-Au complexes; this is beyond the scope of this work.

At $T = 0$ K, QM/MM calculations suggest that the energies involved in the dissociation of a position A C-H bond in a DCA-Au-DCA dimer (by interacting with a DCA(N)---Au-H complex; see SI Figure S16) are approximately twice as large as that for a position A C-H bond in a single DCA molecule. This explains the observation of discrete DCA-Au-DCA dimers and absence of 1D -[DCA-Au-DCA-Au]- organometallic chains.

We claim that the key difference between the previously observed DCA-Cu honeycomb-kagome MOF on Ag(111),[55] and the present study on the organometallic DCA-Au motif is the strength of the metal adatom-cyano interaction. For Cu--N, DFT calculations revealed an interaction energy of $\sim$18.5 kcal/mol ($\sim$0.8 eV), significantly larger than the aforementioned value of 4.2 kcal/mol for Au--N in IS_{2A} (Figure 5c). This favors three-fold Cu-ligand coordination and Cu-based MOF formation, preventing the reaction pathway for C-H bond activation and organometallic bonding as is the case for Au.

Conclusion

We have experimentally observed the formation of organometallic DCA-Au-DCA dimers on a Ag(111) surface at RT. In these dimers, C atoms located specifically at the extremity of

the DCA molecule anthracene moiety (position A) bond covalently to a Au adatom. These observations, supported by DFT, indicate the regioselective C-H bond activation triggered by Au adatoms at RT. Our QM/MM calculations show that this reaction is mediated by the interaction with an intermediate DCA(N)--Au-H metal-organic complex, which significantly reduces the activation barrier of a specific C-H bond. Our work provides atomic-scale insight into selective C-H bond activation, catalyzed by single noble metal atoms and intermediate metal-organic complexes at RT. Our findings have the potential to contribute to addressing the large demand for the synthesis of fuel, fine chemicals and functional organic and organometallic materials. Further investigations could explore such protocols on surfaces or host materials beyond noble metals.

Acknowledgements

Supporting Information

Experimental and theoretical methods; structural characterization of DCA+Au domains; DFT optimized structures; further ncAFM simulations; electronic properties of DCA+Au

dimers; Au adatom character on Ag(111); QM/MM calculations at $T = 0$ K; hybridization and charge distribution across reaction pathway; tentative organometallic dimer formation pathway; secondary C-H activation QM/MM calculations.
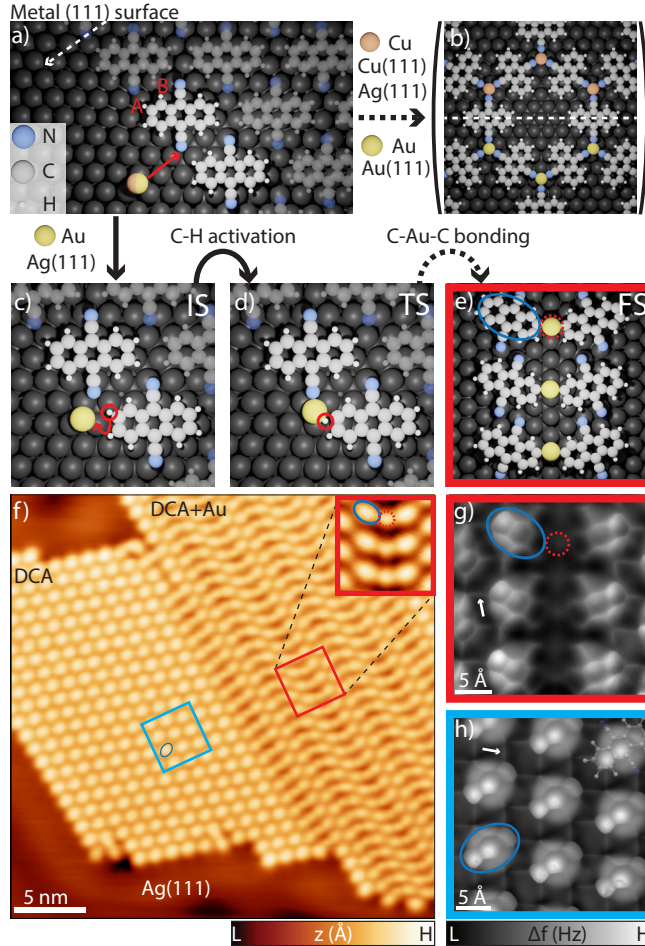
Figure 1: Interactions between noble metal adatoms and cyano-functionalized aromatic molecules on noble metal (111) surfaces: metal-cyano coordination vs. covalent metal-carbon bonding. a) Schematic of 9,10-dicyanoanthracene (DCA) molecules and metal adatoms (Cu or Au) deposited on a (111) noble metal surface (Ag, Cu or Au), with C-H positions A (anthracene end) and B (cyano adjacent) labelled. b) The interaction between DCA and Cu adatoms on Ag(111) or on Cu(111), or with Au adatoms on Au(111), leads to formation of a 2D honeycomb-kagome metal-organic framework (MOF) via three-fold rotationally symmetric metal-cyano coordination.[52–55,58] c)-e) The interaction between DCA and Au adatoms on Ag(111) gives rise to organometallic DCA-Au-DCA dimers via selective (position A) C-H activation and subsequent C-Au covalent bonding (IS: initial state, TS: transition state, FS: final state). f) Constant-current STM image of self-assembled organic DCA-only (DCA) and DCA+Au domains featuring organometallic DCA-Au-DCA dimers on Ag(111) ($V_b = -20$ mV, $I_T = 25$ pA). Inset: high-resolution STM image (same tunneling parameters) of cis organometallic DCA-Au-DCA dimers within DCA+Au self-assembly. Solid blue ellipse: individual DCA molecule. Dashed red circle: Au adatom. g)-h) Constant-height ncAFM images (CO-tip; tip 30 pm closer to the sample with respect to STM setpoint $V_b = 15$ mV, $I_t = 100$ pA) of DCA domain (blue box in f) and of three cis DCA-Au-DCA organometallic dimers in DCA+Au domain (red box in f). White arrows indicate intermolecular N--H interactions.
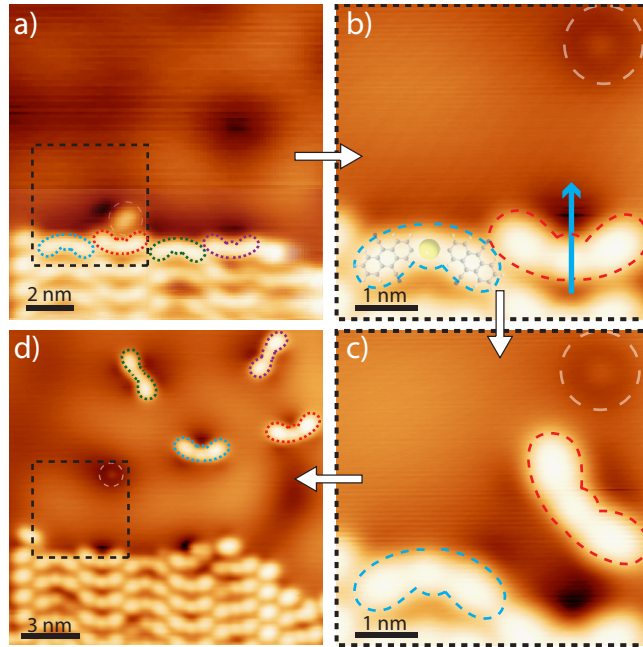
Figure 2: Deconstruction of organometallic DCA+Au self-assembly on Ag(111) via lateral STM manipulation. a)-d) Constant-current STM images showing manipulation of single DCA-Au-DCA units from cis DCA+Au domain [images: $V_b = -20$ mV, $I_t = 10$ pA; manipulation: $V_b = -10$ mV, $I_t = 14$ nA for removal of DCA dimers from 2D film, $V_b = -10$ mV, $I_t = 5$ nA for subsequent translation on Ag(111)]. Blue arrow indicates STM tip path during manipulation. Dashed black square in a) and d) indicates region in b) and c). Dashed outlines indicate manipulated DCA-Au-DCA units. White dashed circles indicate defect adsorbate displaced during manipulation. Ball-and-stick model of DCA-Au-DCA dimer chemical structure overlaid in b).
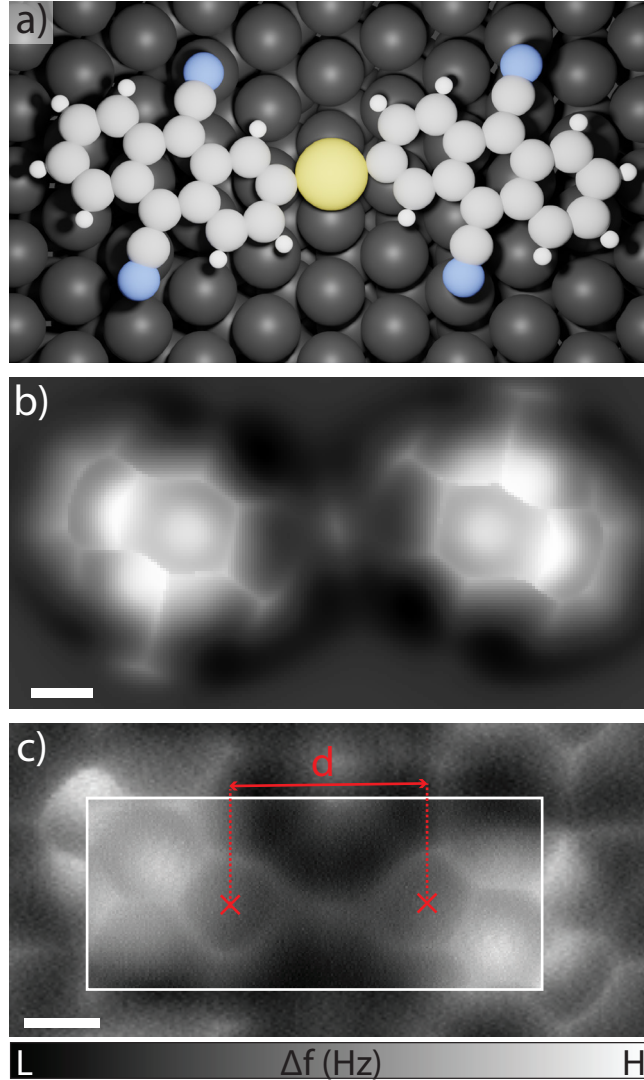
Figure 3: Experimental and theoretical submolecular structure of a trans DCA-Au-DCA pair on Ag(111). a) Ball-and-stick model of DFT-relaxed structure. b) Simulated ncAFM image of optimized structure in a). c) Constant-height (CO-tip) ncAFM image (tip 30 pm closer to the sample with respect to STM setpoint $V_b = 15$ mV, $I_t = 100$ pA). Inset in white box is a higher resolution image taken with the tip 40 pm closer to the surface with respect to the same STM setpoint (see Methods). Red arrow indicates distance, d, between the centers of the benzene rings closest to the Au atom of each DCA molecule involved in an organometallic pair. Simulated image in b): $d_{\text{sim}} = 5.72 \pm 0.06$ Å. Experimental image in c): $d_{\text{exp}} = 6.0 \pm 0.2$ Å. Scale bars: 2.5 Å.
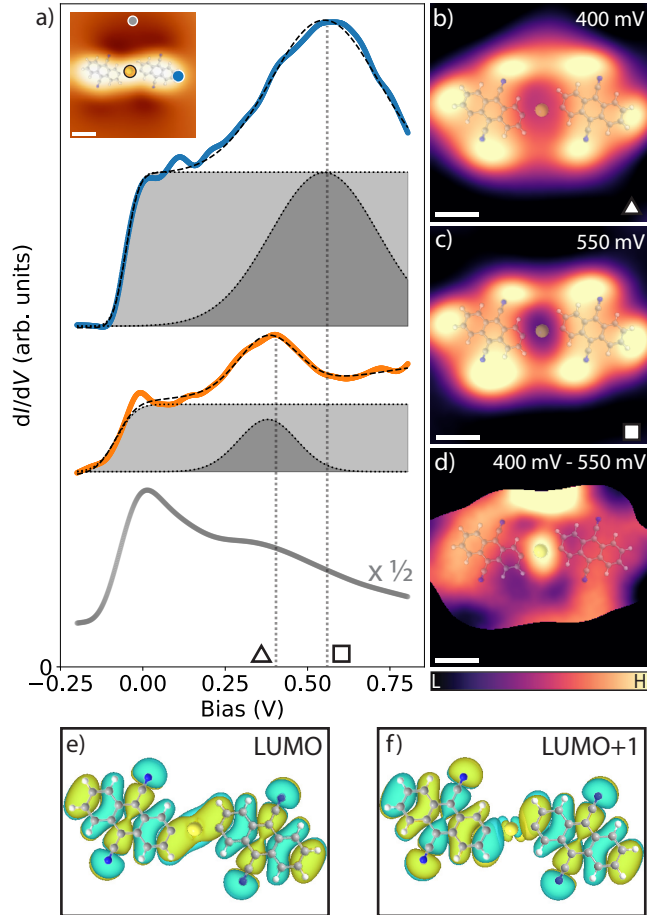
Figure 4: Electronic properties of DCA-Au-DCA organometallic unit. a) dI/dV scanning tunneling spectra obtained at sites indicated in inset (setpoint: $V_b = -200$ mV, $I_t = 20$ pA). Black dashed curves: fits of experimental data consisting of an error function (step-like feature, light gray shaded area), a Gaussian peak (dark gray). An exponential function accounting for tunneling transmission was also included in the fit for the orange curve. Silver reference spectrum (gray curve) scaled down by a factor of 2. Vertical dotted gray lines indicate bias voltages at which dI/dV maps in (b) and (c) were acquired. Inset: constant-current STM image of DCA-Au-DCA unit ($V_b = -20$ mV, $I_t = 50$ pA). b), c) Constant-current dI/dV maps of DCA-Au-DCA unit ($I_t = 500$ pA) at $V_b = 400$ and 550 mV. d) Subtraction between dI/dV maps in b), c) for region corresponding to DCA-Au-DCA unit. DCA-Au-DCA chemical structure overlaid for reference in a) inset and b)-d). Scale bars: 5 Å. We isolated the single DCA-Au-DCA unit from a DCA+Au self-assembled 2D organometallic domain via lateral STM manipulation. e)-f) Wavefunction isosurfaces (0.005 Å$^{-3/2}$; green: positive; blue: negative) for LUMO and LUMO+1 of gas-phase trans DCA-Au-DCA pair calculated by DFT.
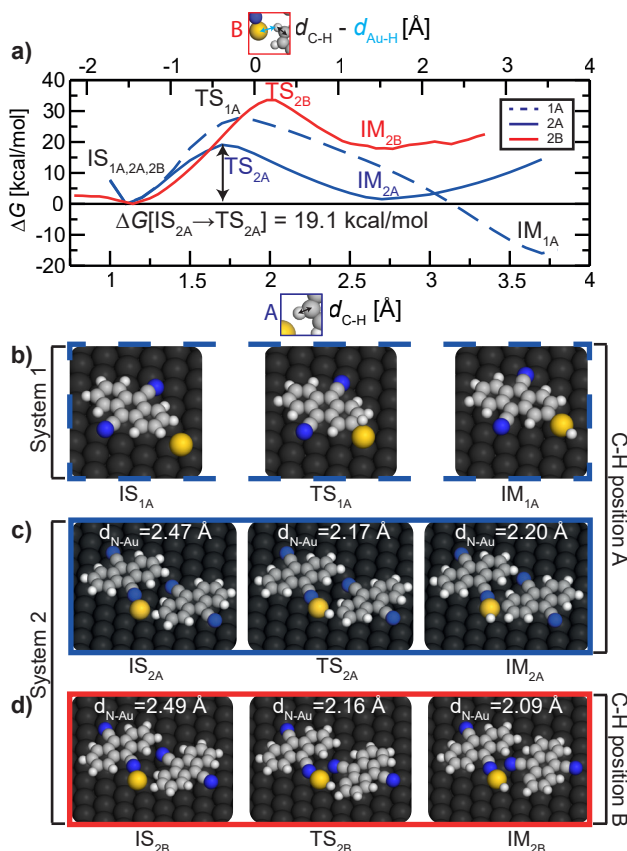
Figure 5: Pathways for Au-induced C-H cleavage of DCA molecule on Ag(111). a) Gibbs free energy differences, ΔG, calculated via QM/MM simulations at $T = 300$ K, for different C-H bond dissociation pathways in a system comprised of a single DCA molecule and a single Au adatom (system 1 in b; dashed curve), and in a system comprised of 2 DCA molecules and a single Au adatom (system 2 in c,d; solid curves). For position A (blue curves), we considered C-H bond length d_{C-H} (bottom axis) as reaction coordinate; for position B (red curve), we considered the difference $(d_{C-H} - d_{Au-H})$ (top axis) between C-H bond length and Au-H distance as reaction coordinate (computationally necessary for this pathway). Activation energy [ΔG between transition (TS) and initial (IS) states] for C-H bond dissociation is reduced for position A in system 2, $\Delta G[IS_{2A} \rightarrow TS_{2A}] = 19.1$ kcal/mol (0.83 eV). b-d) Ball-and-stick models of IS, TS and intermediate (IM) states for C-H bond (positions A and B) dissociation pathways in systems 1 (b) and 2 (c, d).

References

(1) Arndtsen, B. A.; Bergman, R. G.; Mobley, T. A.; Peterson, T. H. Selective Intermolecular Carbon-Hydrogen Bond Activation by Synthetic Metal Complexes in Homogeneous Solution. *Acc. Chem. Res.* **1995**, *28*, 154–162.

(2) Labinger, J. A.; Bercaw, J. E. Understanding and exploiting C–H bond activation. *Nature* **2002**, *417*, 507–514.

(3) Godula, K.; Sames, D. C-H Bond Functionalization in Complex Organic Synthesis. *Science* **2006**, *312*, 67–72.

(4) Crabtree, R. H. Alkane C–H activation and functionalization with homogeneous transition metal catalysts: a century of progress—a new millennium in prospect. *J. Chem. Soc., Dalton Trans.* **2001**, 2437–2450.

(5) Schwach, P.; Pan, X.; Bao, X. Direct Conversion of Methane to Value-Added Chemicals over Heterogeneous Catalysts: Challenges and Prospects. *Chem. Rev.* **2017**, *117*, 8497–8520.

(6) Blaskovits, J. T.; Leclerc, M. C-H Activation as a Shortcut to Conjugated Polymer Synthesis. *Macromolecular Rapid Communications* **2019**, *40*, 1800512.

(7) Yang, Y.; Nishiura, M.; Wang, H.; Hou, Z. Metal-catalyzed CH activation for polymer synthesis and functionalization. *Coordination Chemistry Reviews* **2018**, *376*, 506–532.

(8) Zhang, J.; Kang, L. J.; Parker, T. C.; Blakey, S. B.; Luscombe, C. K.; Marder, S. R. Recent Developments in C–H Activation for Materials Science in the Center for Selective C–H Activation. *Molecules* **2018**, *23*, 922.

(9) Dai, H.-X.; Stepan, A. F.; Plummer, M. S.; Zhang, Y.-H.; Yu, J.-Q. Divergent C–H Functionalizations Directed by Sulfonamide Pharmacophores: Late-Stage Diversification as a Tool for Drug Discovery. *J. Am. Chem. Soc.* **2011**, *133*, 7222–7228.

(10) Jana, R.; Begam, H. M.; Dinda, E. The emergence of the C-H functionalization strategy in medicinal chemistry and drug discovery. *Chem Commun (Camb)* **2021**, *57*, 10842–10866.

(11) Wencel-Delord, J.; Glorius, F. C–H bond activation enables the rapid construction and late-stage diversification of functional molecules. *Nature Chemistry* **2013**, *5*, 369–375.

(12) Zhang, L.; Ritter, T. A Perspective on Late-Stage Aromatic C–H Bond Functionalization. *J. Am. Chem. Soc.* **2022**, *144*, 2399–2414.

(13) Cernak, T.; Dykstra, K. D.; Tyagarajan, S.; Vachal, P.; Krska, S. W. The medicinal chemist's toolbox for late stage functionalization of drug-like molecules. *Chem. Soc. Rev.* **2016**, *45*, 546–576.

(14) Yamaguchi, J.; Yamaguchi, A. D.; Itami, K. C-H Bond Functionalization: Emerging Synthetic Tools for Natural Products and Pharmaceuticals. *Angewandte Chemie International Edition* **2012**, *51*, 8960–9009.

(15) Dutta, U.; Maiti, S.; Bhattacharya, T.; Maiti, D. Arene diversification through distal C(sp2)-H functionalization. *Science* **2021**, *372*, eabd5992.

(16) Ramadoss, B.; Jin, Y.; Asako, S.; Ilies, L. Remote steric control for undirected meta-selective C-H activation of arenes. *Science* **2022**, *375*, 658–663.

(17) Xue, X.-S.; Ji, P.; Zhou, B.; Cheng, J.-P. The Essential Role of Bond Energetics in C–H Activation/Functionalization. *Chem. Rev.* **2017**, *117*, 8622–8648.

(18) Tiwari, V. K.; Kapur, M. Catalyst-controlled positional-selectivity in C–H functionalizations. *Org. Biomol. Chem.* **2019**, *17*, 1007–1026.

(19) Shilov, A. E.; Shul'pin, G. B. Activation of C-H Bonds by Metal Complexes. *Chem. Rev.* **1997**, *97*, 2879–2932.

(20) Labinger, J. A. Platinum-Catalyzed C–H Functionalization. *Chem. Rev.* **2017**, *117*, 8483–8496.

(21) Lewis, J. C.; Coelho, P. S.; Arnold, F. H. Enzymatic functionalization of carbon–hydrogen bonds. *Chem. Soc. Rev.* **2011**, *40*, 2003–2021.

(22) Clair, S.; de Oteyza, D. G. Controlling a Chemical Coupling Reaction on a Surface: Tools and Strategies for On-Surface Synthesis. *Chem. Rev.* **2019**, *119*, 4717–4776.

(23) Fan, Q.; Gottfried, J. M.; Zhu, J. Surface-Catalyzed C–C Covalent Coupling Strategies toward the Synthesis of Low-Dimensional Carbon-Based Nanostructures. *Acc. Chem. Res.* **2015**, *48*, 2484–2494.

(24) Grill, L.; Hecht, S. Covalent on-surface polymerization. *Nat. Chem.* **2020**, *12*, 115–130.

(25) Held, P. A.; Fuchs, H.; Studer, A. Covalent-Bond Formation via On-Surface Chemistry. *Chemistry – A European Journal* **2017**, *23*, 5874–5892.

(26) Mishra, S.; Beyer, D.; Eimre, K.; Kezilebieke, S.; Berger, R.; Gröning, O.; Pignedoli, C. A.; Müllen, K.; Liljeroth, P.; Ruffieux, P.; Feng, X.; Fasel, R. Topological frustration induces unconventional magnetism in a nanographene. *Nature Nanotechnology* **2020**, *15*, 22–28.

(27) Mishra, S.; Beyer, D.; Eimre, K.; Ortiz, R.; Fernandez-Rossier, J.; Berger, R.; Groening, O.; Pignedoli, C. A.; Fasel, R.; Feng, X.; Ruffieux, P. Collective All-Carbon Magnetism in Triangulene Dimers. *Angewandte Chemie International Edition* **2020**, *59*, 12041–12047.

(28) Pavliček, N.; Mistry, A.; Majzik, Z.; Moll, N.; Meyer, G.; Fox, D. J.; Gross, L. Synthesis and characterization of triangulene. *Nature Nanotechnology* **2017**, *12*, 308–311.

(29) Su, J. et al. Atomically precise bottom-up synthesis of Pi-extended [5]triangulene. *Science Advances* **2019**, *5*, 7717.

(30) Cai, J.; Ruffieux, P.; Jaafar, R.; Bieri, M.; Braun, T.; Blankenburg, S.; Muoth, M.; Seitsonen, A. P.; Saleh, M.; Feng, X.; Müllen, K.; Fasel, R. Atomically precise bottom-up fabrication of graphene nanoribbons. *Nature* **2010**, *466*, 470–473.

(31) Rizzo, D. J.; Veber, G.; Cao, T.; Bronner, C.; Chen, T.; Zhao, F.; Rodriguez, H.; Louie, S. G.; Crommie, M. F.; Fischer, F. R. Topological band engineering of graphene nanoribbons. *Nature* **2018**, *560*, 204–208.

(32) Ruffieux, P.; Wang, S.; Yang, B.; Sánchez-Sánchez, C.; Liu, J.; Dienel, T.; Talirz, L.; Shinde, P.; Pignedoli, C. A.; Passerone, D.; Dumslaff, T.; Feng, X.; Müllen, K.; Fasel, R. On-surface synthesis of graphene nanoribbons with zigzag edge topology. *Nature* **2016**, *531*, 489–492.

(33) Cirera, B.; Sánchez-Grande, A.; de la Torre, B.; Santos, J.; Edalatmanesh, S.; Rodríguez-Sánchez, E.; Lauwaet, K.; Mallada, B.; Zbořil, R.; Miranda, R.; Gröning, O.; Jelínek, P.; Martín, N.; Ecija, D. Tailoring topological order and Pi- conjugation to engineer quasi-metallic polymers. *Nature Nanotechnology* **2020**, *15*, 437–443.

(34) Sánchez-Grande, A.; de la Torre, B.; Santos, J.; Cirera, B.; Lauwaet, K.; Chutora, T.; Edalatmanesh, S.; Mutombo, P.; Rosen, J.; Zbořil, R.; Miranda, R.; Björk, J.; Jelínek, P.; Martín, N.; Écija, D. On-Surface Synthesis of Ethynylene-Bridged Anthracene Polymers. *Angewandte Chemie International Edition* **2019**, *58*, 6559–6563.

(35) Galeotti, G. et al. Synthesis of mesoscale ordered two-dimensional Pi-conjugated polymers with semiconducting properties. *Nat. Mater.* **2020**, *19*, 874–880.

(36) Springer, M. A.; Liu, T.-J.; Kuc, A.; Heine, T. Topological two-dimensional polymers. *Chem. Soc. Rev.* **2020**, *49*, 2007–2019.

(37) Fan, Q.; Werner, S.; Tschakert, J.; Ebeling, D.; Schirmeisen, A.; Hilt, G.; Hieringer, W.; Gottfried, J. M. Precise Monoselective Aromatic C–H Bond Activation by Chemisorption of Meta-Aryne on a Metal Surface. *J. Am. Chem. Soc.* **2018**, *140*, 7526–7532.

(38) Li, Q.; Yang, B.; Lin, H.; Aghdassi, N.; Miao, K.; Zhang, J.; Zhang, H.; Li, Y.; Duhm, S.; Fan, J.; Chi, L. Surface-Controlled Mono/Diselective ortho C–H Bond Activation. *J. Am. Chem. Soc.* **2016**, *138*, 2809–2814.

(39) Lackinger, M. Surface-assisted Ullmann coupling. *Chem. Commun.* **2017**, *53*, 7872–7885.

(40) Giannakakis, G.; Flytzani-Stephanopoulos, M.; Sykes, E. C. H. Single-Atom Alloys as a Reductionist Approach to the Rational Design of Heterogeneous Catalysts. *Acc. Chem. Res.* **2019**, *52*, 237–247.

(41) Mitchell, S.; Pérez-Ramírez, J. Single atom catalysis: a decade of stunning progress and the promise for a bright future. *Nat Commun* **2020**, *11*, 4302.

(42) Parkinson, G. S. Single-Atom Catalysis: How Structure Influences Catalytic Performance. *Catal Lett* **2019**, *149*, 1137–1146.

(43) Wang, A.; Li, J.; Zhang, T. Heterogeneous single-atom catalysis. *Nat Rev Chem* **2018**, *2*, 65–81.

(44) Böhme, D. K.; Schwarz, H. Gas-Phase Catalysis by Atomic and Cluster Metal Ions: The Ultimate Single-Site Catalysts. *Angewandte Chemie International Edition* **2005**, *44*, 2336–2354.

(45) Zhong, D.; Franke, J.-H.; Podiyanachari, S. K.; Blömker, T.; Zhang, H.; Kehr, G.; Erker, G.; Fuchs, H.; Chi, L. Linear Alkane Polymerization on a Gold Surface. *Science* **2011**, *334*, 213–216.

(46) Lafferentz, L.; Eberhardt, V.; Dri, C.; Africh, C.; Comelli, G.; Esch, F.; Hecht, S.; Grill, L. Controlling on-surface polymerization by hierarchical and substrate-directed growth. *Nature Chem* **2012**, *4*, 215–220.

(47) Blunt, M. O.; Russell, J. C.; Champness, N. R.; Beton, P. H. Templating molecular adsorption using a covalent organic framework. *Chem. Commun.* **2010**, *46*, 7157–7159.

(48) Zhang, H.; Franke, J.-H.; Zhong, D.; Li, Y.; Timmer, A.; Arado, O. D.; Mönig, H.; Wang, H.; Chi, L.; Wang, Z.; Müllen, K.; Fuchs, H. Surface Supported Gold–Organic

Hybrids: On-Surface Synthesis and Surface Directed Orientation. *Small* **2014**, *10*, 1361–1368.

(49) Xing, S.; Zhang, Z.; Fei, X.; Zhao, W.; Zhang, R.; Lin, T.; Zhao, D.; Ju, H.; Xu, H.; Fan, J.; Zhu, J.; Ma, Y.-q.; Shi, Z. Selective on-surface covalent coupling based on metal-organic coordination template. *Nat Commun* **2019**, *10*, 70.

(50) Karan, S.; Geng, Y.; Decurtins, S.; Liu, S.-X.; Repp, J. Gold-linked strings of donor–acceptor dyads: on-surface formation and mutual orientation. *Chem. Commun.* **2020**, *56*, 7901–7904.

(51) Kumar, D.; Krull, C.; Yin, Y.; Medhekar, N. V.; Schiffrin, A. Electric Field Control of Molecular Charge State in a Single-Component 2D Organic Nanoarray. *ACS Nano* **2019**, *13*, 11882–11890.

(52) Pawin, G.; Wong, K. L.; Kim, D.; Sun, D.; Bartels, L.; Hong, S.; Rahman, T. S.; Carp, R.; Marsella, M. A Surface Coordination Network Based on Substrate-Derived Metal Adatoms with Local Charge Excess. *Angewandte Chemie International Edition* **2008**, *47*, 8442–8445.

(53) Zhang, J.; Shchyrba, A.; Nowakowska, S.; Meyer, E.; Jung, T. A.; Muntwiler, M. Probing the spatial and momentum distribution of confined surface states in a metal coordination network. *Chem. Commun.* **2014**, *50*, 12289–12292.

(54) Hernández-López, L.; Piquero-Zulaica, I.; Downing, C. A.; Piantek, M.; Fujii, J.; Serrate, D.; Ortega, J. E.; Bartolomé, F.; Lobo-Checa, J. Searching for kagome multi-bands and edge states in a predicted organic topological insulator. *Nanoscale* **2021**, *13*, 5216–5223.

(55) Kumar, D.; Hellerstedt, J.; Field, B.; Lowe, B.; Yin, Y.; Medhekar, N. V.; Schiffrin, A. Manifestation of Strongly Correlated Electrons in a 2D Kagome Metal–Organic Framework. *Advanced Functional Materials* **2021**, *31*, 2106474.

(56) Yan, L.; Silveira, O. J.; Alldritt, B.; Krejčí, O.; Foster, A. S.; Liljeroth, P. Synthesis and Local Probe Gating of a Monolayer Metal-Organic Framework. *Advanced Functional Materials* **2021**, *31*, 2100519.

(57) Yan, L.; Silveira, O. J.; Alldritt, B.; Kezilebieke, S.; Foster, A. S.; Liljeroth, P. Two-Dimensional Metal–Organic Framework on Superconducting NbSe2. *ACS Nano* **2021**, *15*, 17813–17819.

(58) Yan, L.; Pohjavirta, I.; Alldritt, B.; Liljeroth, P. On-Surface Assembly of Au-Dicyanoanthracene Coordination Structures on Au(111). *ChemPhysChem* **2019**, *20*, 2297–2300.

(59) Arras, E.; Seitsonen, A. P.; Klappenberger, F.; Barth, J. V. Nature of the attractive interaction between proton acceptors and organic ring systems. *Phys. Chem. Chem. Phys.* **2012**, *14*, 15995–16001.

(60) Zhang, X.; Xue, N.; Li, C.; Li, N.; Wang, H.; Kocić, N.; Beniwal, S.; Palotás, K.; Li, R.; Xue, Q.; Maier, S.; Hou, S.; Wang, Y. Coordination-Controlled C–C Coupling Products via ortho-Site C–H Activation. *ACS Nano* **2019**, *13*, 1385–1393.

(61) Pawlak, R.; Liu, X.; Ninova, S.; D'Astolfo, P.; Drechsel, C.; Sangtarash, S.; Häner, R.; Decurtins, S.; Sadeghi, H.; Lambert, C. J.; Aschauer, U.; Liu, S.-X.; Meyer, E. Bottom-up Synthesis of Nitrogen-Doped Porous Graphene Nanoribbons. *J. Am. Chem. Soc.* **2020**, *142*, 12568–12573.

(62) Li, Q.; Yang, B.; Björk, J.; Zhong, Q.; Ju, H.; Zhang, J.; Cao, N.; Shi, Z.; Zhang, H.; Ebeling, D.; Schirmeisen, A.; Zhu, J.; Chi, L. Hierarchical Dehydrogenation Reactions on a Copper Surface. *J. Am. Chem. Soc.* **2018**, *140*, 6076–6082.

(63) Fan, D.; Sakai, Y.; Chelikowsky, J. R. Chemical and steric effects in simulating non-contact atomic force microscopy images of organic molecules on a Cu (111) substrate. *Phys. Rev. Materials* **2020**, *4*, 053802.

(64) Kumagai, T.; Hanke, F.; Gawinkowski, S.; Sharp, J.; Kotsis, K.; Waluk, J.; Persson, M.; Grill, L. Controlling intramolecular hydrogen transfer in a porphycene molecule with single atoms or molecules located nearby. *Nature Chem* **2014**, *6*, 41–46.

(65) Hapala, P.; Kichin, G.; Wagner, C.; Tautz, F. S.; Temirov, R.; Jelínek, P. Mechanism of high-resolution STM/AFM imaging with functionalized tips. *Phys. Rev. B* **2014**, *90*, 085421.

(66) Li, J.; Schneider, W.-D.; Berndt, R. Local density of states from spectroscopic scanning-tunneling-microscope images: Ag(111). *Phys. Rev. B* **1997**, *56*, 7656–7659.

(67) Liljeroth, P.; Swart, I.; Paavilainen, S.; Repp, J.; Meyer, G. Single-Molecule Synthesis and Characterization of Metal-Ligand Complexes by Low-Temperature STM. *Nano Lett.* **2010**, *10*, 2475–2479.

(68) Liu, X.; Matej, A.; Kratky, T.; Mendieta-Moreno, J. I.; Günther, S.; Mutombo, P.; Decurtins, S.; Aschauer, U.; Repp, J.; Jelinek, P.; Liu, S.-X.; Patera, L. L. Exploiting Cooperative Catalysis for the On-Surface Synthesis of Linear Heteroaromatic Polymers via Selective C–H Activation. *Angewandte Chemie International Edition* **2022**, *61*, e202112798.

(69) Sun, Q.; Zhang, C.; Kong, H.; Tan, Q.; Xu, W. On-surface aryl–aryl coupling via selective C–H activation. *Chem. Commun.* **2014**, *50*, 11825–11828.

(70) Liu, J.; Chen, Q.; He, Q.; Zhang, Y.; Fu, X.; Wang, Y.; Zhao, D.; Chen, W.; Xu, G. Q.; Wu, K. Bromine adatom promoted C–H bond activation in terminal alkynes at room temperature on Ag(111). *Phys. Chem. Chem. Phys.* **2018**, *20*, 11081–11088.

(71) Telychko, M.; Su, J.; Gallardo, A.; Gu, Y.; Mendieta-Moreno, J. I.; Qi, D.; Tadich, A.; Song, S.; Lyu, P.; Qiu, Z.; Fang, H.; Koh, M. J.; Wu, J.; Jelínek, P.; Lu, J. Strain-Induced Isomerization in One-Dimensional Metal–Organic Chains. *Angewandte Chemie International Edition* **2019**, *58*, 18591–18597.

(72) Han, D.; Tao, Z.; Wang, T.; Feng, L.; Li, X.; Zeng, Z.; Zhu, J. Sequential Activation of Aromatic C-H Bonds on Cu(111). *J. Phys. Chem. C* **2022**, *126*, 5541–5549.

(73) Zeng, Z.; Guo, D.; Wang, T.; Chen, Q.; Matěj, A.; Huang, J.; Han, D.; Xu, Q.; Zhao, A.; Jelínek, P.; de Oteyza, D. G.; McEwen, J.-S.; Zhu, J. Chemisorption-Induced Formation of Biphenylene Dimer on Ag(111). *J. Am. Chem. Soc.* **2022**, *144*, 723–732.

Supporting Information: Selective Activation of Aromatic C-H Bonds Catalyzed by Single Gold Atoms at Room Temperature

Benjamin Lowe,[†,‡,⊥] Jack Hellerstedt,[†,‡,⊥] Adam Matěj,[¶,§,∥,⊥] Pingo Mutombo,[¶] Dhaneesh Kumar,[†,‡] Martin Ondráček,[¶] Pavel Jelinek,*,[¶,§] and Agustin Schiffrin*,[†,‡]

†School of Physics and Astronomy, Monash University, Clayton, Victoria 3800, Australia

‡ARC Centre for Excellence in Low-Energy Electronics Technologies, Monash University, Clayton, Victoria 3800, Australia

¶Institute of Physics, Academy of Sciences of the Czech Republic, Cukrovarnická 10, 1862 53, Prague, Czech Republic

§Regional Centre of Advanced Technologies and Materials, Czech Advanced Technology and Research Institute (CATRIN), Palacký University Olomouc, 779 00 Olomouc, Czech Republic

∥Department of Physical Chemistry, Faculty of Science, Palacký University Olomouc, 771 46 Olomouc, Czech Republic

⊥Contributed equally to this work

E-mail: jelinekp@fzu.cz; agustin.schiffrin@monash.edu

Contents

S1   Experimental methods

S1.1   Sample preparation

The DCA+Au system was synthesized in UHV (base pressure 2×10^{-10} mbar) by co-deposition of DCA molecules (Tokyo Chemical Industry; >95% purity) and Au (>99.99% purity) from the gas phase onto a clean Ag(111) surface held at room temperature (RT). The Ag(111) surface was cleaned by 2-3 cycles of sputtering with Ar^+ ions and subsequent annealing at ~500ºC. The DCA molecules (Au atoms, deposited simultaneously) were sublimated at 120ºC (1040ºC, respectively). The sample was held at RT for a further 1 hour before sample characterization. We also performed preparations with equivalent parameters in which DCA molecules then Au atoms were deposited sequentially. Both methods yielded qualitatively similar samples.

S1.2   STM and STS measurements

All STM and dI/dV STS measurements were performed at 4.5 K (base pressure $< 1 \times 10^{-10}$ mbar) with a hand-cut Pt/Ir tip. All STM images were acquired in constant-current mode with tunneling parameters as reported in the text (bias voltage applied to sample). All dI/dV spectra were obtained by acquiring $I(V)$ as a function of bias voltage at a constant tip-sample distance (stabilized by a specified setpoint tunneling current and bias voltage), and by then numerically differentiating $I(V)$ to obtain dI/dV as a function of bias voltage. All dI/dV maps were acquired in constant-current mode (using setpoints $I_t = 500$ pA and bias voltages as specified), with a lock-in technique by modulating the bias voltage with an amplitude of 10 mV at a frequency of 1.13 kHz, except the dI/dV map in Figure S5b) (non-covalent DCA-only dimer) which was acquired via a single bias slice of the numerical derivative of pixel-by-pixel $I(V)$ curves.

S1.3 NcAFM measurements

All ncAFM measurements were performed at 4.5 K in UHV (base pressure $< 1 \times 10^{-10}$ mbar) with a qPlus tuning fork sensor ($f_0 \approx 30$ kHz, $Q \approx 66$k, $K \approx 1.8$ kNm^{-1}, 50 pm amplitude modulation) with a CO-terminated Pt/Ir tip, in constant-height mode at a tip-sample distance defined by a STM setpoint (as specified in main text). The Pt/Ir tip was functionalized with a CO molecule by dosing CO gas into the UHV chamber (5×10^8 mbar for 3 seconds) with the sample held at a temperature below 7 K. For functionalization, the tip was brought above a CO molecule adsorbed on Ag(111) at a height defined by the STM setpoint $V_b = 20$ mV, $I_t = 25$ pA. The tip was then lowered 375 pm to 'pick-up' the molecule before tunneling feedback was restored. Confirmation of symmetrical adsorption of CO at the tip apex was obtained by imaging other CO molecules on Ag(111) with the functionalized tip. CO molecules appearing in STM images as circular protrusions surrounded by an isotropic depression indicated successful symmetric CO-functionalization of the tip.

S1.4 STM lateral manipulation

All lateral manipulation experiments were conducted with an Ag-terminated Pt/Ir STM tip at temperatures below 5 K. To remove individual DCA-Au-DCA dimers from the self-assembled DCA+Au domains, a tip-sample distance was defined by tunneling parameters $V_B = -10$ mV, $I_t = 14$ nA at a site in between DCA-Au-DCA dimers within the DCA+Au domain [start of blue arrow in main text Figure 2b)]. The tip was then translated laterally at a speed of 200 pm/s along paths specified in images. Once removed from the DCA+Au domain, we performed further lateral manipulation using a tip-sample distance defined by the tunneling parameters $V_B = -10$ mV, $I_t = 5$ nA above bare Ag(111) to move the DCA-Au-DCA units about the surface at the same tip speed.

S2   Theoretical methods

S2.1   Gas-phase density functional theory (DFT) calculations

Bond dissociation enthalpies (BDE), ΔH, for gas phase DCA [Figure S7a)] were calculated by density functional theory (DFT) with the Gaussian16 package,[1] using the ωB97X-D functional[2] with the def2-SVP basis set.[3]

We also carried out DFT calculations using the FHI-AIMS code[4] to investigate the electronic properties and total energy of certain DCA complexes in the gas phase. We performed these calculations at the B3LYP level,[5] using the Tkatchenko-Scheffler treatment of the van der Waals interactions.[6] This method was used for calculations shown in sections S6 and S9 below.

S2.2   On-surface DFT calculations: electronic structure, total energy

We carried out DFT calculations using the FHI-AIMS code[4] to investigate the electronic properties and total energy of DCA and its complexes on both Ag(111) and Au(111) surfaces. We performed these calculations at the GGA-PBE[7] level, using the Tkatchenko-Scheffler treatment of the van der Waals interactions.[6] As Ag(111) and Au(111) surfaces, we employed a 5×11 supercell with three atomic layers (see SI Figure S6). All atoms of the supercell structure were structurally relaxed except for the bottom layer furthest from the adsorbates. Convergence was achieved when atomic force and total energy differences were below 10^{-2} eV/Å and 10^{-5} eV, respectively. We used a single Γ point to sample the Brillouin zone.

S2.3 Hybrid quantum mechanics/molecular mechanics (QM/MM) calculations

We employed quantum mechanics/molecular mechanics (QM/MM) simulations to calculate total energy differences, ΔE, and Gibbs free energy differences, ΔG, for different systems composed of DCA molecules and Au atoms adsorbed on Ag(111) (see main text Figure 5, and Figures S7, S8, S16), at $T = 0$ and 300 K. We used the umbrella sampling method to calculate ΔG along different reaction pathways. We employed Sander[8] as the main program with Fireball[9] as the code for QM calculations. The QM calculations with Fireball used the BLYP[5,10] exchange correlation functional with D3 corrections,[11] and a basis set consisting of optimized numerical atomic-like orbitals,[12] i.e., s orbital for H, sp^3 orbitals for C and N, and sp^3d^5 for Au and Ag. The accuracy of the QM/MM Fireball-Sander method has been previously benchmarked with QM/MM Gaussian-Sander simulations using B3LYP[5,13,14]/def2-SVP, validating the use of Fireball in these conditions.[15]

In main text Figure 5, the reaction coordinate for the umbrella sampling of ΔG was set along the C-H bond of interest for the systems in panels b) and c); for the system in panel d), the reaction coordinate was defined as the difference between the lengths of C-H and Au-H bonds involved in the reaction. For each reaction pathway, ΔG was calculated by: (i) starting from the transition state TS determined beforehand, the system was steered both towards the initial state IS as well as the intermediate state IM; at each frame the system was relaxed (structurally and electronically) via DFT with an applied restraint on the reaction coordinate (with $T = 0$ K); (ii) the system was then tempered from 0 to 300 K via a molecular dynamics (MD) simulations of 600 time steps of 0.5 fs; (iii) finally, a set of MD simulations was submitted for each frame with 5000 time steps of 0.5 fs. The ΔG profiles were obtained by collecting the restrained bond lengths at each step and via a weighted histogram analysis method.

S2.4 NcAFM simulations

The simulations of the ncAFM images [main text Figure 3b); Figure S3) were based on the probe-particle model[16] which includes van der Waals (vdW) and electrostatic interactions between the CO tip and the surface. All simulations were performed with a charge scaling of $-1e$ at the probe apex and a probe lateral stiffness (k) of 0.25 N/m. The electrostatic forces were obtained based on the Hartree potential calculated from the total energy FHI-AIMS DFT calculations.

S3 DCA+Au domains: structural characterization

Figure S1 shows STM and ncAFM topographic images of self-assembled DCA+Au domains with cis (a) and trans (b-e) DCA-Au-DCA units. We determined the registration of the DCA+Au domains with respect to the substrate by atomically resolved imaging of bare Ag(111) [top of Figure S1d), e); red circles indicate Ag atom positions] and by subsequently extrapolating the Ag(111) atomic lattice within the DCA+Au domains, showing the adsorption position of the DCA-Au-DCA units. The self-assembled DCA+Au domains are incommensurate with the Ag(111) surface, with unit cell vectors [$\mathbf{b_1}$, $\mathbf{b_2}$ in Figure S1b)] forming an angle of 5.0 ± 0.5º with respect to the Ag(111) unit cell vectors. The cis and trans domain configurations have equivalent lattice vectors, with $\mathbf{a_1}$ being ∼twice as long as $\mathbf{b_1}$ to account for the alternating orientations of the cis DCA-Au-DCA units. We also sporadically observed bright ncAFM features at the center of some of the DCA-Au-DCA units [indicated by dashed circles in Figure S1c)-e)]. We claim that these are likely adsorbed residual gas molecules. We tentatively suspect they may be CO molecules (deliberately introduced for ncAFM) based on observations of inadvertent tip functionalization during manipulation experiments.
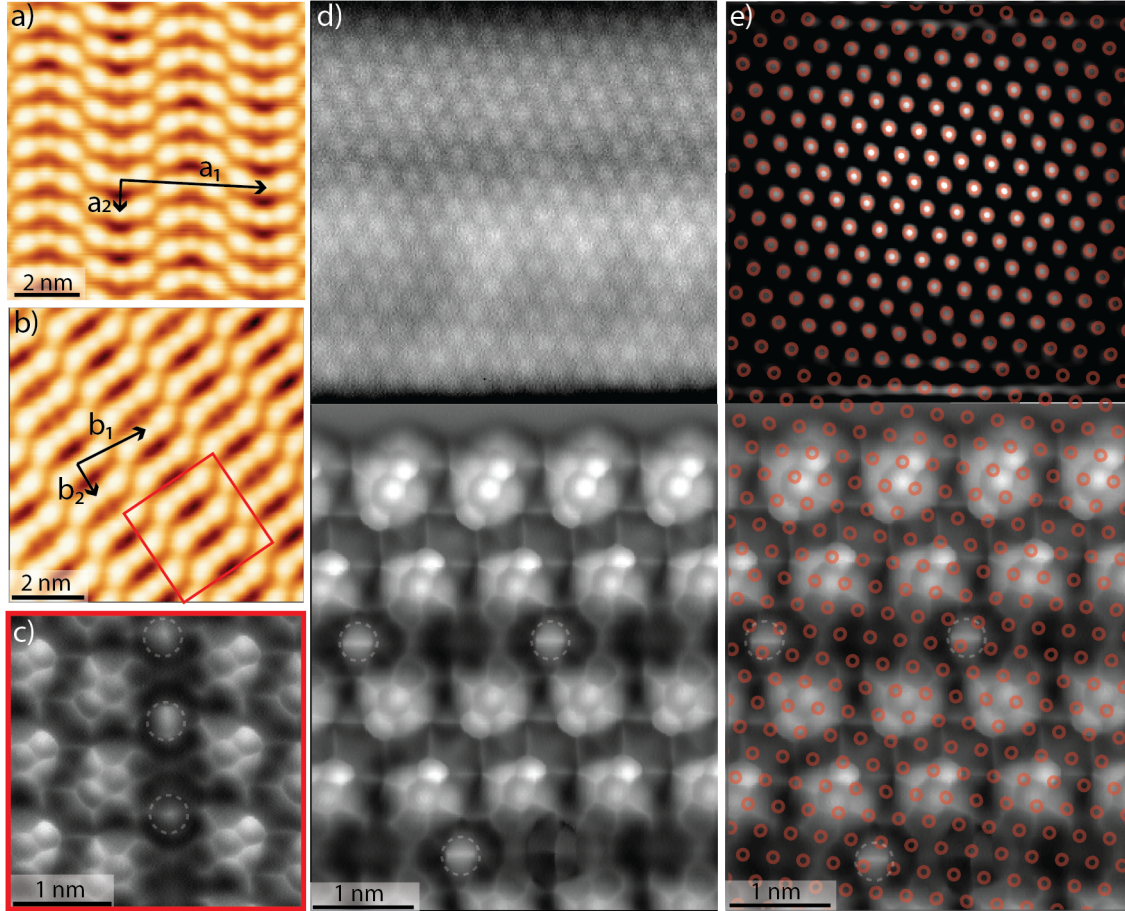
Figure S1: Organometallic DCA-Au-DCA dimers in self-assembled DCA+Au domains on Ag(111). a)-b) Constant-current STM images with cis ($I_t = 25$ pA) and trans ($I_t = 10$ pA) DCA-Au-DCA dimers, respectively ($V_b = -20$ mV). Vectors $\mathbf{a}_1$ and $\mathbf{a}_2$, and $\mathbf{b}_1$ and $\mathbf{b}_2$ define primitive unit cell vectors of the 2D domains ($a_1 = 4.38 \pm 0.05$ nm, $a_2 = 0.97 \pm 0.05$ nm, $b_1 = 2.08 \pm 0.05$ nm, $b_2 = 1.05 \pm 0.05$ nm). c) CO-tip constant-height ncAFM image of region of trans DCA+Au domain shown in the red box in b) (tip 30 pm closer to sample with respect to STM setpoint $V_b = 15$ mV, $I_t = 100$ pA). d)-e) CO-tip constant-height ncAFM image of trans DCA+Au domain boundary. Top: Atomically resolved bare Ag(111) area (tip height defined by STM setpoint $V_b = 3$ mV, $I_t = 700$ pA). Bottom: trans DCA-Au-DCA dimers (tip 30 pm closer to sample with respect to STM setpoint $V_b = 15$ mV, $I_t = 100$ pA). e) Same as d), with Fourier filtering of the bare Ag(111) region to emphasize the atomic lattice. Red circles indicate Ag atom positions [based on bare Ag(111) at the top] allowing us to determine the DCA+Au domain registration with respect to the substrate. Sporadic bright features at the center of some of the DCA-Au-DCA units in c)-e) (indicated by dashed circles) are likely adsorbed residual gas molecules.

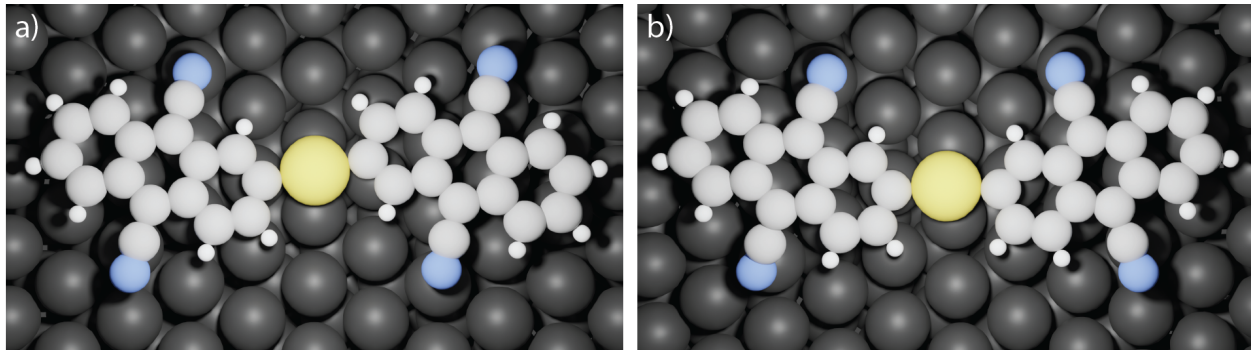# S4 Structure of DCA-Au-DCA units: DFT

Figure S2: Ball-and-stick schematic of structure of DFT-relaxed trans (a) and cis (b) DCA-Au-DCA dimers on Ag(111) (see Section S2.2). The total energy difference between the two configurations is only ~0.2 kcal/mol which indicates that both are similarly stable, consistent with their observed coexistence in experiments.

S5 NcAFM imaging simulations

Figure S3 shows a comparison between simulated and experimental ncAFM images of organometallic DCA-Au-DCA and organic DCA-DCA (i.e., covalently bonded via position A carbon atoms) units. The simulated ncAFM image for a DFT-relaxed DCA-Au-DCA dimer [Figure S3a)] shows good qualitative agreement with the experimental image [Figure S3g)], with a reduced frequency shift Δf for the benzene rings closest to the Au atom (i.e., darker appearance) in comparison to the other DCA benzene rings, and the experimentally measured distance $d \approx 6.0$ Å between the centers of these benzene rings similar to $d \approx 5.72$ Å in the simulation. Importantly, the simulated ncAFM image of an hypothesized DCA-DCA dimer (with a covalent C-C bond between position A carbon atoms) fails to qualitatively capture such experimentally observed features, with a significantly larger Δf at the DCA-DCA linkage and significantly smaller $d \approx 4.76$ Å. These findings support our claim that the experimentally observed Au-induced structure consist of an organometallic DCA-Au-DCA dimers featuring a covalent C-Au-C bonding motif. Since purely organic molecular domains were observed when only DCA molecules were deposited on Ag(111) (i.e., without Au de-

position),[17] we also claim that Ag atoms from the Ag(111) surface do not play a role in the formation of the DCA-Au-DCA dimer motif.
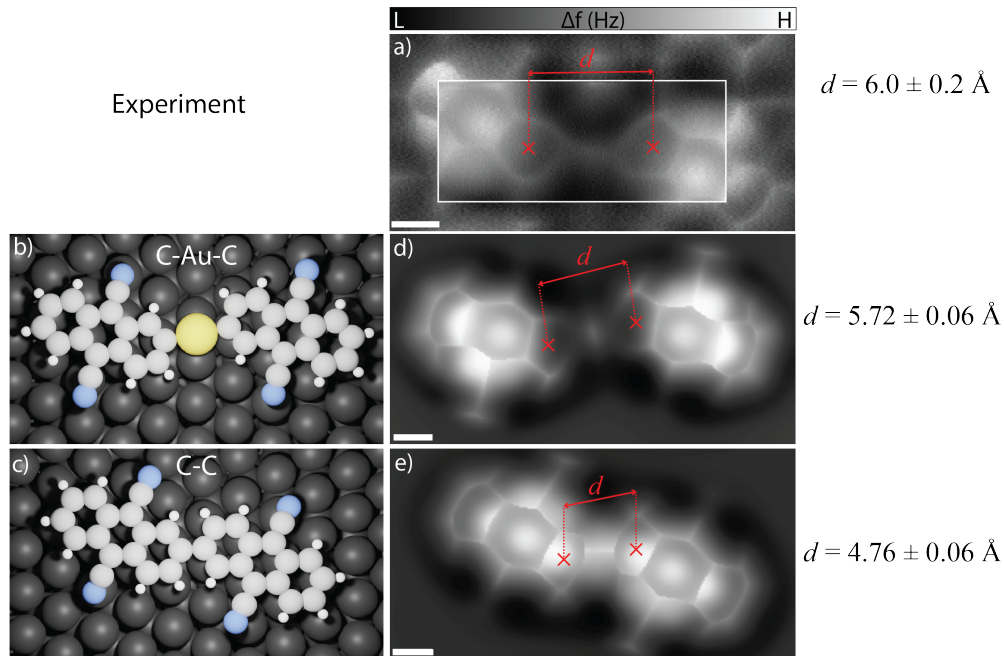

Figure S3: Comparison of experimental and simulated ncAFM images. a) Experimental constant-height ncAFM image of DCA-Au-DCA dimer, acquired with a CO-functionalized tip (tip 30 pm closer to sample with respect to STM setpoint $V_b = 15$ mV, $I_t = 100$ pA), showing good agreement with simulated ncAFM image in d), in particular regarding the distance d between the centres of the two benzene rings closest to the Au atom. b), c) Ball-and-stick models of DFT structurally optimized DCA-Au-DCA and DCA-DCA dimers on Ag(111) (see Section S2.2). d), e) Probe-particle ncAFM simulations for structures in (b, c).

S6 Electronic properties of DCA-Au-DCA dimers

Figure S4 shows the projected density of states (PDOS) of a gas-phase DCA-Au-DCA dimer as calculated by DFT (see Methods), with contributions from DCA and Au states (top), and specifically from Au 5d states (bottom). The calculated LUMO and LUMO+1 have predominantly DCA character, with a small contribution from the Au $5d_{yz}$ orbital, consistent with the experimental dI/dV maps in Figure 4 of the main text. The spatial distribution of these states, both experimentally [Figure 4b), c) in main text] and theoretically [Figure 4e),

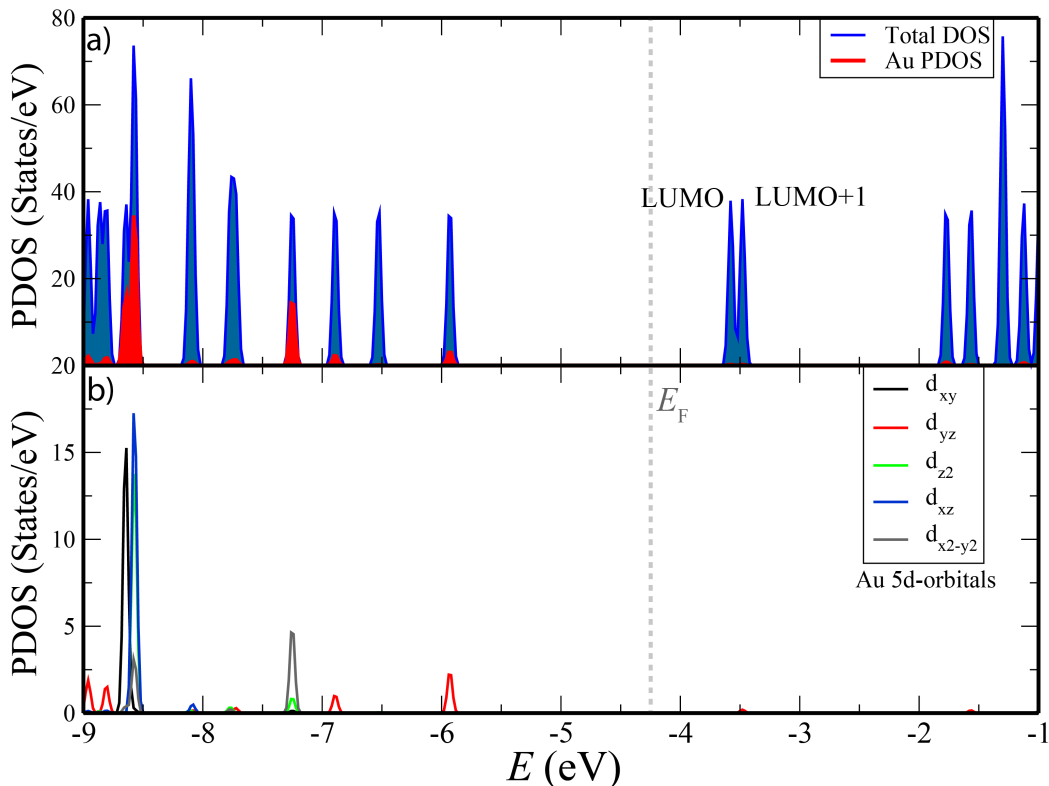f) in main text], is similar to that of the previously observed DCA LUMO.[17]

Figure S4: Projected density of states (PDOS) of gas-phase DCA-Au-DCA dimer calculated by DFT (B3LYP), as a function of energy. a) Total density of states (blue) and Au PDOS (red). b) PDOS onto Au 5d orbitals. Dashed grey line indicates position of Fermi level (E_F). This electronic structure calculation is related to Figure 4e-f) in main text.

Figure S5 shows dI/dV spectra and maps for an organic, non-covalently bonded DCA-only dimer and for an organometallic DCA-Au-DCA dimer [data for the latter are the same as in main text Figure 4a-c)]. The dI/dV spectrum taken at the anthracene end of the DCA-only dimer [red curve in Figure S5a)] shows a peak at $V_b \approx 0.47$ V attributed to the DCA LUMO, as observed previously.[17] In contrast, spectra for the organometallic DCA-Au-DCA dimer [blue and orange curves in Figure S5a), b)] show a peak at lower energy ($V_b \approx 0.38$ V) and a peak at higher energy ($V_b \approx 0.56$ V), that we attribute to the LUMO and LUMO+1 of the DCA-Au-DCA system (see main text). Based on this and on the predominantly molecular character of these LUMO and LUMO+1 determined via DFT (Figure S4), we

claim that these molecular states of the DCA-Au-DCA dimer are the result of hybridization between the two DCA LUMOs mediated by the DCA-Au covalent bonding.
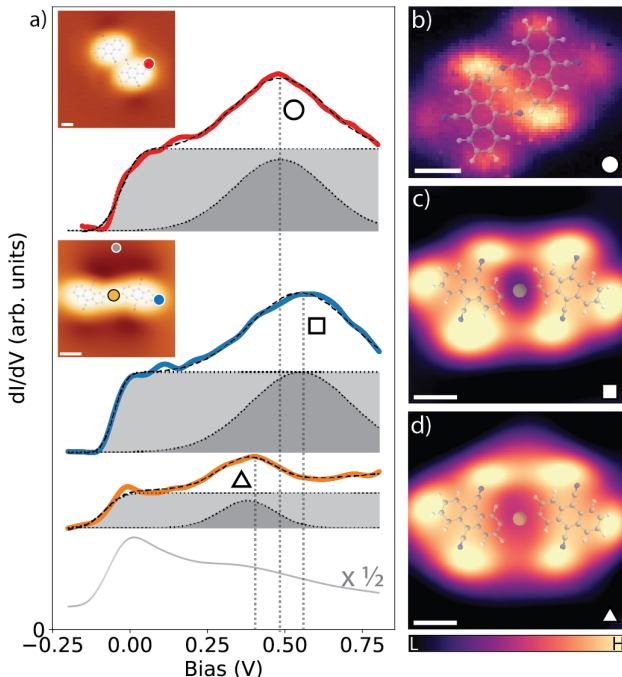

Figure S5: Electronic properties of organic DCA-only dimer and organometallic DCA-Au-DCA dimer on Ag(111). a) $\mathrm{d}I/\mathrm{d}V$ spectra for DCA-only dimer (red), DCA-Au-DCA dimer (blue, orange) and bare Ag(111) (gray), acquired at sites indicated in insets. Setpoints: V_b = -200 mV, I_t = 20 pA [DCA-Au-DCA; Ag(111)]; V_b = -200 mV, I_t = 10 pA (DCA-only; see Methods). Curves offset for clarity. Grey shaded regions are fits (error function plus Gaussian peak) of experimental data. Insets: constant-current STM images of DCA-only (top) and DCA-Au-DCA (bottom) dimers (V_b = -20 mV, I_t = 50 pA). b) Slice of pixel-by-pixel $\mathrm{d}I/\mathrm{d}V$ curves obtained via the numerical derivative of $I(V)$ curves (setpoint V_b = -200 mV, I_t = 1 pA) at a bias of 486 mV. c) - d) $\mathrm{d}I/\mathrm{d}V$ maps (constant current I_t = 500 pA) at 400 and 550 mV, respectively, for an organometallic DCA-Au-DCA structure (constant-current lock-in method). All scale bars: 5 Å.

S7 Au adatom character on Ag(111): DFT

Figure S6a) shows the density of states (PDOS), projected onto Au 5d states, of an Au adatom on Ag(111) and on Au(111), as a function of energy. This PDOS was calculated via DFT at the B3LYP level (see Method). The PDOS for Au on Ag(111) is a lot sharper than on Au(111). The energy broadening of the adatom Au 5d states on Au(111) is indicative of

significant electronic hybridization between adatom and surface, while the sharp PDOS on Ag(111) shows that the electronic character of Au on Ag(111) is close to that of an isolated neutral Au atom.
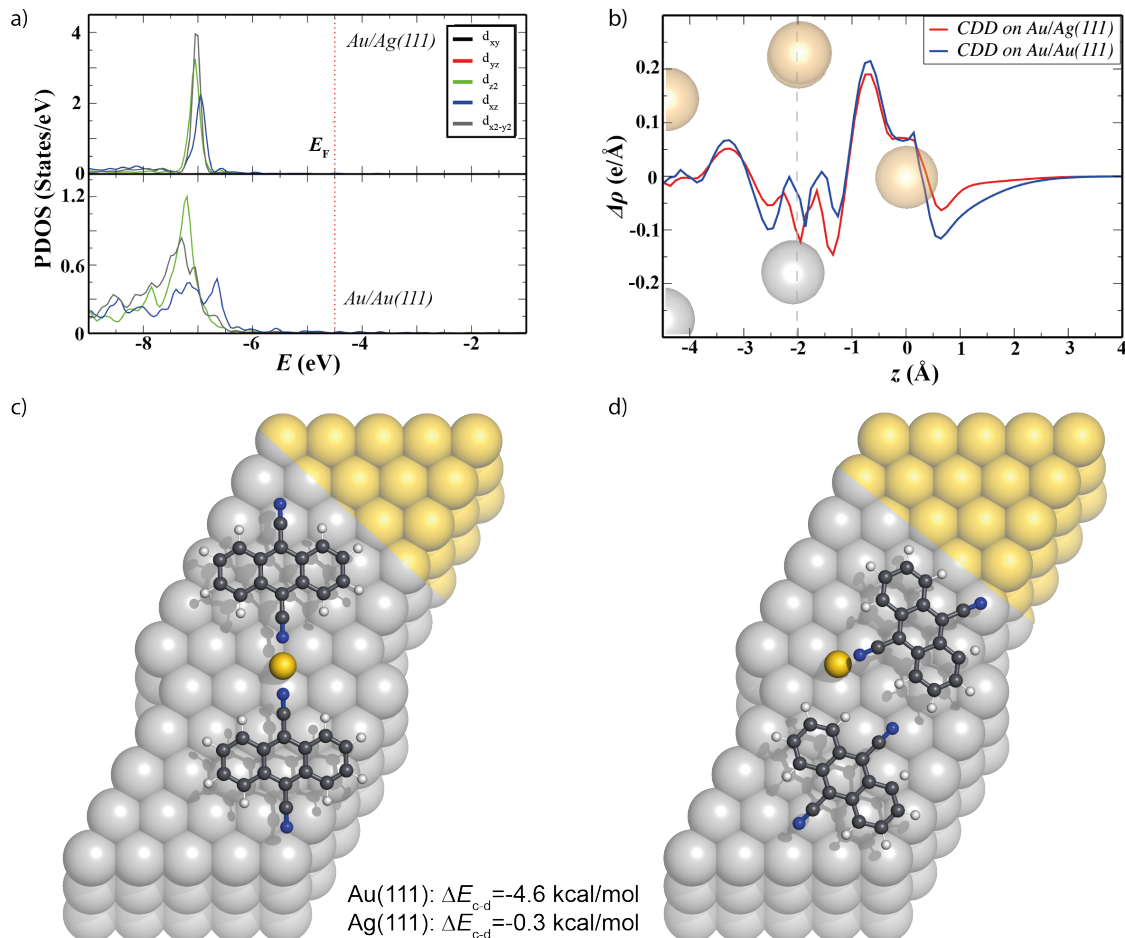

Figure S6: (a) Projected density of states (PDOS) onto Au 5d states for Au adatom on Ag(111) and on Au(111), as a function of energy, calculated via DFT (GGA-PBE). Energy broadening of the adatom Au 5d states on Au(111) is indicative of significant hybridization with the surface, while the sharp PDOS on Ag(111) indicates that the electronic character of Au on Ag(111) is close to that of an isolated neutral Au atom. (b) 1D projected charge density difference, $\Delta\rho$, for Au adatom on Au(111) (blue curve) and on Ag(111) (red curve), as a function of coordinate z normal to the surface. Au adatom position corresponds to $z = 0$. Dashed vertical line indicates position of top-most layer of Ag(111) and Au(111). c), d) Ball-and-stick schematics of two different metal-organic complexes on Au(111) and Ag(111), consisting of 2 DCA molecules coordinated to an Au adatom via their nitrogen atoms. Total energy differences, ΔE, between complexes in c) and d), on Au(111) and Ag(111), calculated by DFT (GGA-PBE).

We considered the total energy (calculated via DFT at the GGA-PBE level; see Methods) of different metal-organic complexes on both Au(111) and Ag(111) [Figure S6c), d)]. These complexes consisted of 2 DCA molecules coordinated to an Au adatom via their cyano N atoms, in different configurations.

On Au(111), the configuration where the Au adatom is coordinated to the cyano groups of the two DCA molecules in a linear geometry [Figure S6c)] is 4.6 kcal/mol more stable than the configuration where the Au adatom is coordinated to the cyano group of one DCA and interacts with the hydrogen atoms of the other [Figure S6d)]. On Ag(111), this difference is reduced to a negligible 0.3 kcal/mol. That is, different configurations of cyano-coordinated DCA-Au complexes with similar total energies might co-exist on Ag(111). In contrast, cyano-Au interactions dominate on Au(111). This provides an explanation for the difference between our present study and the previously observed honeycomb-kagome metal-organic framework on Au(111) where DCA and Au adatoms are coordinated via the DCA cyano groups.[18]

These different configurations of energetically similar, cyano-coordinated DCA-Au complexes on Ag(111) suggest that a dynamic equilibrium between different metal-organic phases could be present at room temperature. This dynamic equilibrium could then evolve irreversibly towards the experimentally observed DCA-Au-DCA dimers (via the regioselective C-H activation mechanism discussed in the main text and below).

S8   C-H bond dissociation energies: QM/MM calculations

In Figure S7, we considered two different C-H bond dissociation mechanisms in a system composed of a single DCA molecule and a single Au adatom on Ag(111) (system 1 in main text): one involving the interaction between Au and the position A C-H bond [Figure S7b-d)]; the other involving the interaction between Au and the position B C-H bond [Figure

S7e-g)]. Note that the C-H bond dissociation enthalpies (BDE) for positions A and B in gas phase DCA are very similar [Figure S7a)]. The experimentally observed regioselectivity of the C-H bond cleavage therefore cannot be explained by differences in BDE. We performed QM/MM simulations (at $T = 0$ K first) to calculate the total energy differences, ΔE, along these two reaction pathways, as an initial estimate of activation barriers. These calculations yielded similar energy differences between transition (TS) and initial (IS) states of 50.2 and 52.9 kcal/mol for positions A and positions B, respectively. This C-H bond dissociation mechanism mediated by a single Au adatom interacting with a single DCA molecule therefore also fails to explain the selectivity of the C-H scission at position A observed in experiments.
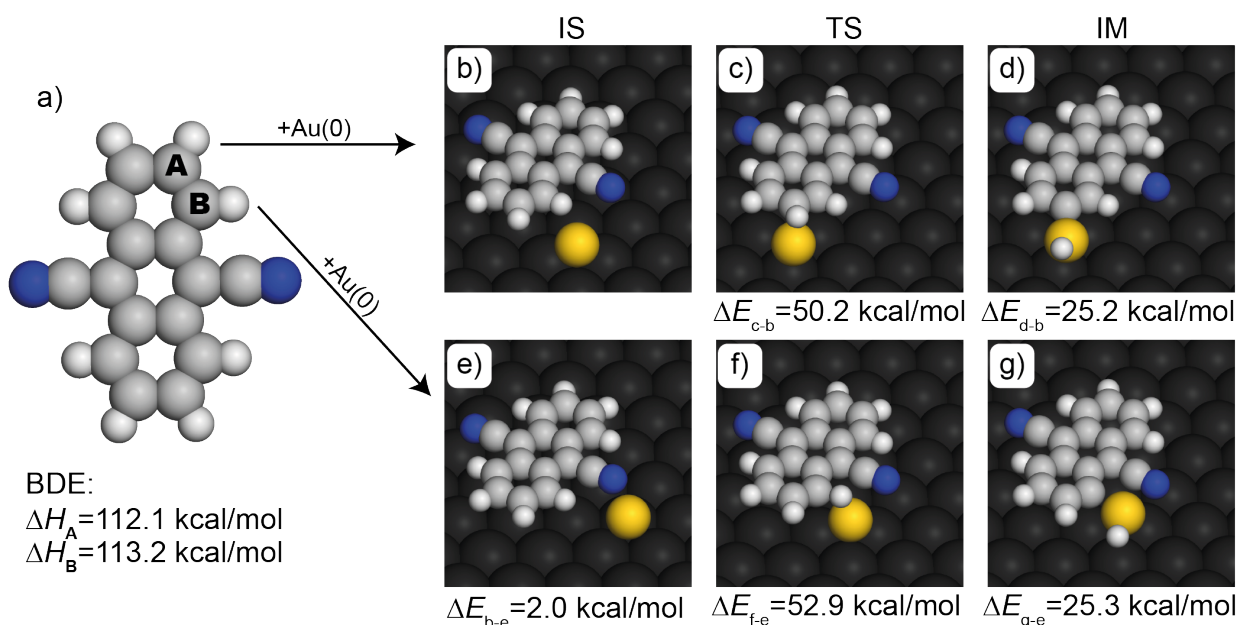

Figure S7: Different pathways for C-H bond cleavage in a single DCA molecule induced by a single Au adatom on Ag(111): QM/MM calculations at $T = 0$ K. a) Ball-and-stick structure of gas-phase DCA, with positions A and B C-H bond dissociation enthalpies (BDE), $\Delta H_{\mathrm{A,B}}$, calculated via DFT (see Methods). b) - g) Ball-and-stick models of initial (IS), transition (TS) and intermediate (IM) states along positions A (b - d) and B (e - g) C-H bond dissociation pathways, with total energy differences ΔE calculated via QM/MM simulations at $T = 0$ K.

We then performed QM/MM calculations at $T = 0$ K for similar C-H dissociation processes for a system composed of two DCA molecules and a single Au adatom on Ag(111) (Figure S8; system 2 in main text). Interestingly, these calculations show that C-H bond

dissociation pathways that involve a TS where DCA coordinates to Au via a metal-ligand bond at one of its cyano N atoms yield a substantially reduced energy difference ΔE between TS and IS ($\approx$30 kcal/mol) for the C-H activation of an adjacent DCA molecule, for both positions A [Figure S8b), e)] and B [Figure S8c), f)]. While these calculations do not support the experimentally observed regioselectivity either, the lowering of these energy differences does suggest that a metal-organic cyano-Au motif may facilitate C-H bond cleaving.
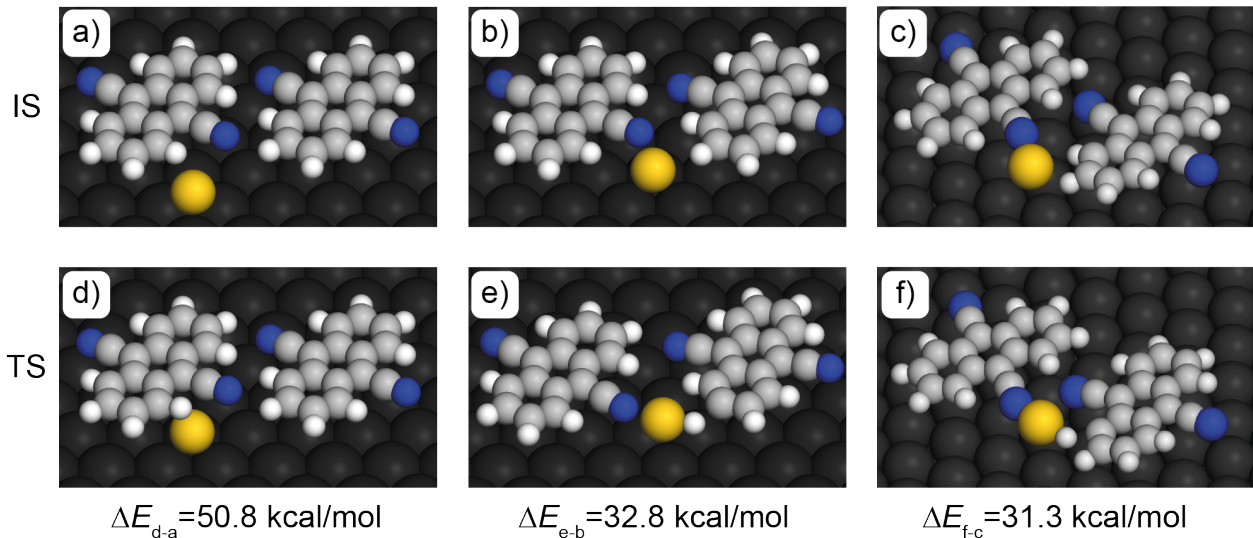

Figure S8: QM/MM calculated total energy differences, ΔE, at $T = 0$ K between TS and IS for systems containing two DCA molecules and a single Au atom on Ag(111). A significant reduction in the energy difference is observed when a TS consisting of a metal-organic DCA-Au complex (with a N--Au coordination bond) is formed, for both positions A and B.

These findings motivated the QM/MM calculations at $T = 300$ K (i.e., close to our experimental conditions; see Methods) shown in the main text. These QM/MM calculations allowed us to determine the Gibbs free energy differences ΔG (and hence the activation barriers, defined as ΔG between transition and initial states) for the considered C-H bond dissociation pathways. That is, the total energy differences ΔE above and ΔG are strictly not identical, although they are related, with $\Delta E(T = 0)$ providing an initial estimate of ΔG.

S9 Orbital hybridization in reaction pathway

The QM/MM calculations reveal a significant lowering of the C-H dissociation barrier in DCA on Ag(111), when DCA interacts with a DCA--Au complex (in which Au forms a metal-organic coordination bond with a cyano N atoms). This interaction gives rise to an intermediate metal-organic H-Au--(N)DCA complex (with a linear H-Au--N motif) and to a DCA· radical (with a cleaved anthracene extremity C-H bond; Figure S8).

In the following, we focus on the electronic properties of the H-Au--(N)DCA intermediate, and present a hypothetical mechanism that explains the lowering of the DCA C-H bond activation barrier via such an intermediate. We calculated (via DFT at the B3LYP level; see Methods) the density of states (DOS) and projected DOS (PDOS) of three different isolated systems to analyze the nature of the bonding between Au and DCA in this intermediate: H-Au (Figure S9), Au--(N)DCA (Figure S10) and H-Au--(N)DCA (S11).

We first considered the DOS of H-Au (Figure S9). The total DOS reveals three molecular orbitals of hybrid Au and H character. Projecting the density of states of these three orbitals onto the Au atomic orbitals reveals they have predominantly $5d_{z2}$, 6s and $6p_z$ character as well as H 1s character. We identify these orbitals as bonding (σ), non-bonding (nb) and anti-bonding (σ^*) orbitals.

We then considered the DOS of a Au--(N)DCA system (Figure S10). In contrast to the findings for Au-H, the calculated DOS of this system reveals very little hybridization of Au states. Figure S10b) shows the PDOS onto Au atomic orbitals (solid lines) relative to PDOS for an isolated, neutral Au atom (dashed lines). All Au orbitals are shifted upwards in energy by the proximity to DCA, but their relative energies and appearance in the PDOS are fundamentally unchanged. This suggests negligible hybridization due to Au--N bonding, and no bonding or antibonding orbitals are formed. The interaction energy between Au and DCA in the complex is small ($\sim$4 kcal/mol), pointing to a weak interaction via polarization and electrostatics. Figure S10d) shows the charge density difference, which reveals a significant local polarization of the Au atom due to the proximity of the cyano group. This local

polarization causes intra-atomic charge redistribution within the Au atom. In particular, we observe electron accumulation in a ring surrounding the Au atom (green isosurface), balanced by electron depletion (pink) along the Au-cyano axis. Importantly, there is electron depletion on the outside of the Au atom, in the direction from which a H atom could approach to form the intermediate DCA(H)-Au--(N)DCA complex (see IM$_{2A}$ in main text and below). The depleted density on the Au adatom reduces the Pauli repulsion between the Au and H atoms. This facilitates the formation of a chemical bond between Au and H.

Lastly, we considered the DOS of a H-Au--(N)DCA system (Figure S11). In Figure S11 we find that the σ, nb and σ^* orbitals seen for Au-H are preserved for this system. This can be clearly seen in the comparison between Au-H and H-Au--(N)DCA DOS shown in Figure S12. In the case of H-Au--(N)DCA, however, σ and σ^* orbitals undergo further hybridization with the N orbitals of DCA which results in further splitting of the σ^* orbital. While this Au-N hybridization is still relatively minor and does not support the claim of a dative bond, the interaction energy between Au and N increases significantly (by $\sim$22 kcal/mol) for this system, with a corresponding reduction in Au--N distance of $\sim$0.5 Å, relative to the Au--(N)DCA system.
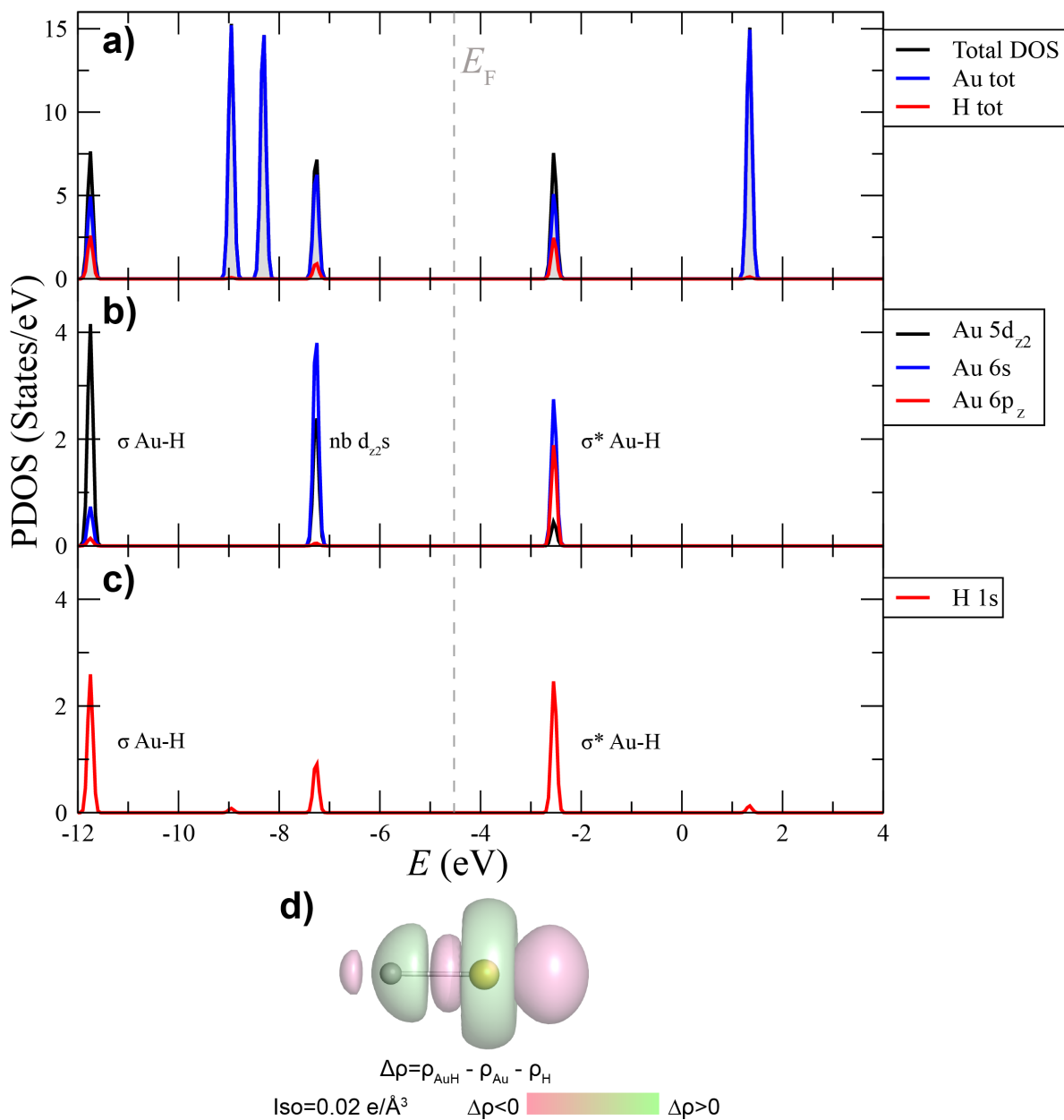
Figure S9: Density of states (DOS) and orbital character of isolated Au-H system, calculated via DFT (B3LYP). (a) Total DOS (black curve with gray filling) and projected DOS (PDOS; blue: onto Au states; red: onto H states), as a function of energy. (b) PDOS projected onto Au $5d_{z2}$, Au 6s and Au $6p_z$ orbitals, as a function of energy. (c) PDOS onto H 1s states. Au-H system bonding (σ), antibonding (σ) orbitals, and non-bonding (nb) d_{z2}s hybrid orbital are indicated. (d) Electron density difference $\Delta\rho$ between Au-H system, and neutral isolated Au(0) atom and neutral isolated H atom.
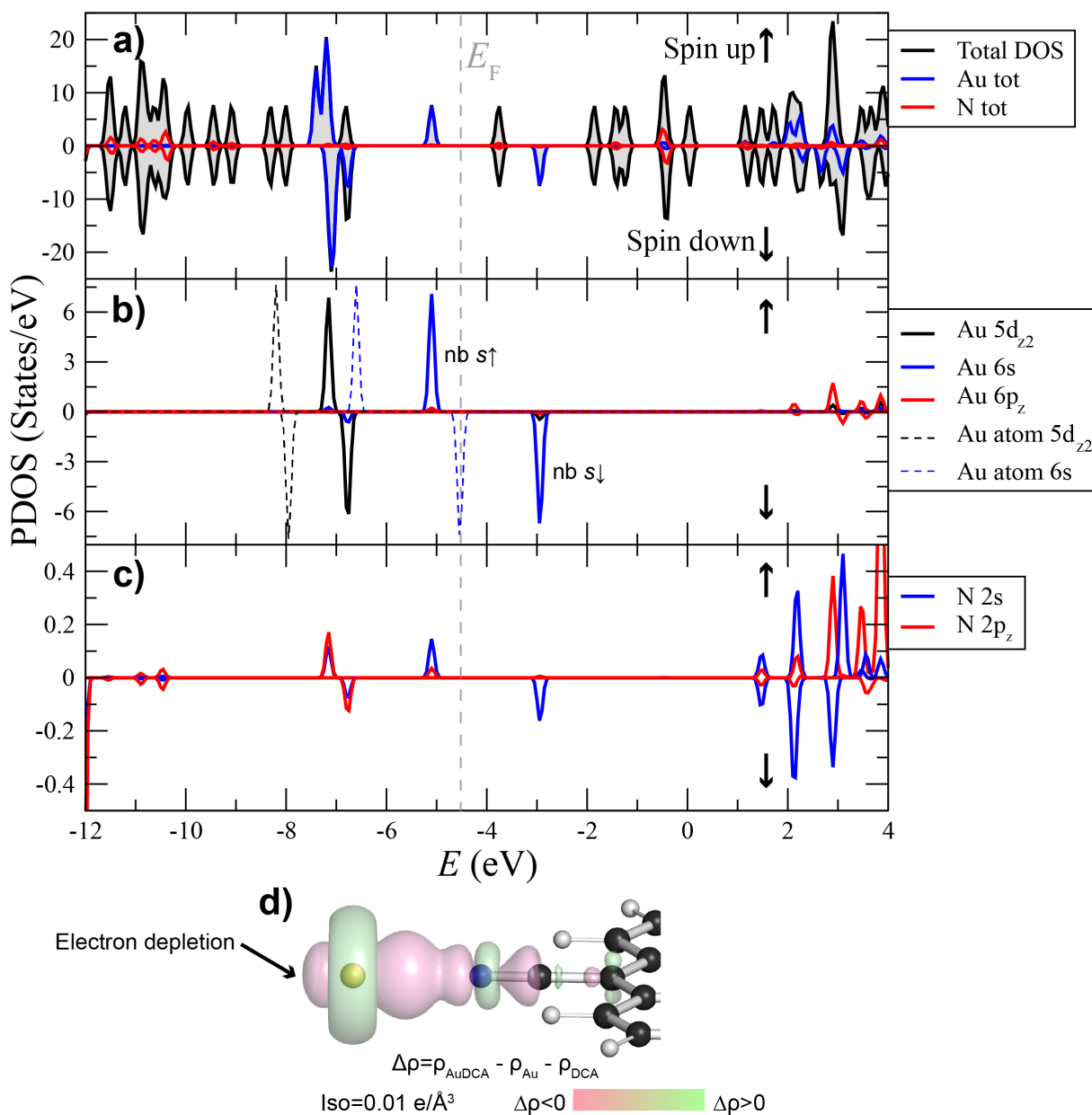
Figure S10: Density of states (DOS) and orbital character of Au--(N)DCA system, calculated via DFT (B3LYP). (a) Total DOS (black with gray filling) and projected DOS (PDOS; blue: onto Au states; red: onto states of N atom coordinated with Au), as a function of energy. (b) PDOS, projected onto Au $5d_{z2}$, 6s and $6p_z$ orbitals, as function of energy. Dashed curves correspond to an isolated neutral Au atom, for comparison. (c) PDOS onto N 2s and $2p_z$ orbitals. (d) Electron density difference $\Delta\rho$ between Au--(N)DCA, and neutral isolated Au(0) atom and neutral isolated DCA. Spin degeneracy lifting shown for this figure as the net electronic structure is open-shell (not the case for other figures in this section).
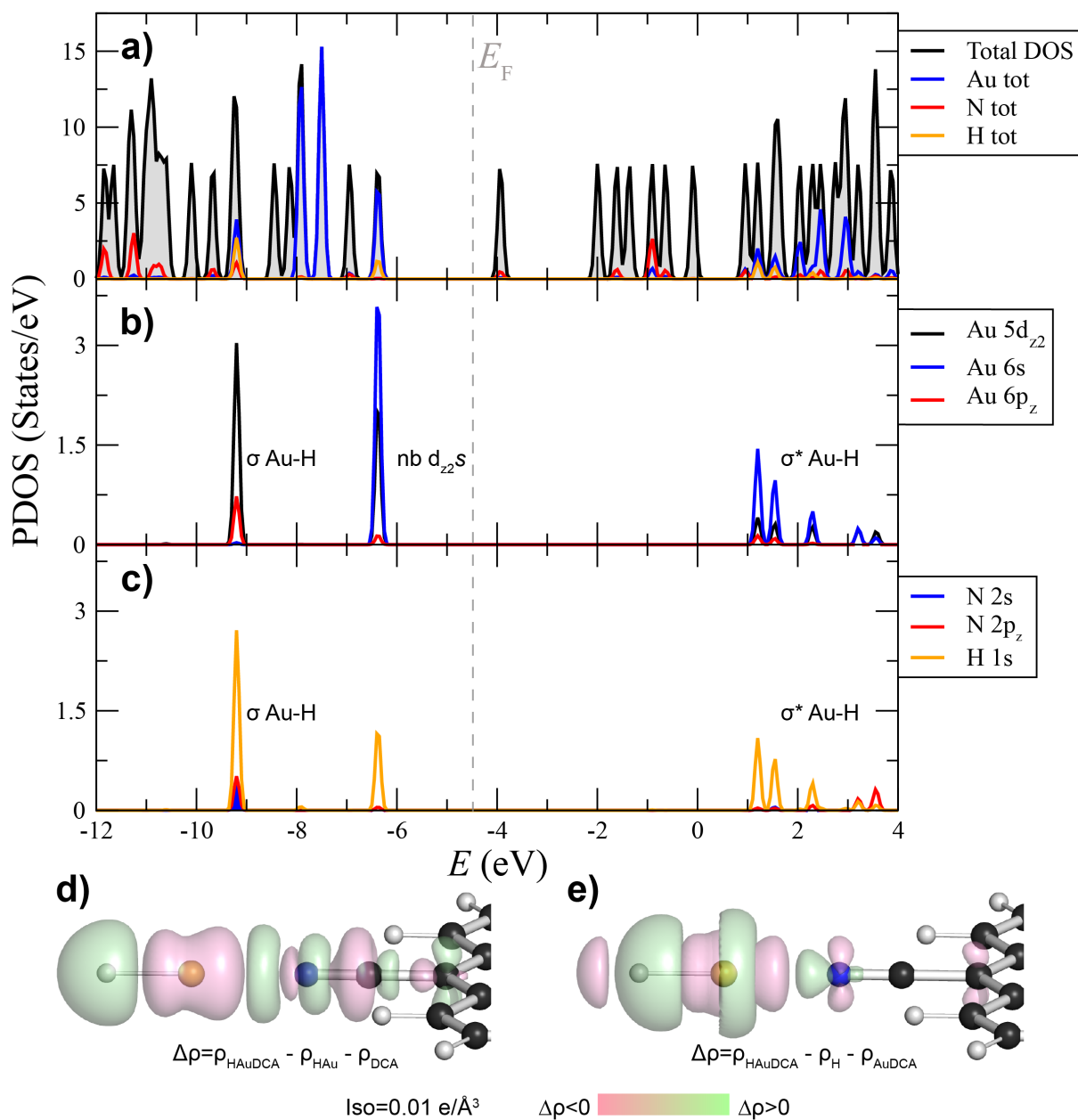
Figure S11: Density of states (DOS) and orbital character of H-Au--(N)DCA system, calculated via DFT (B3LYP). (a) Total DOS (black with gray filling) and projected DOS (PDOS; blue: onto Au states; red: onto states of N atom coordinated with Au; orange: onto states of H atom coordinated with Au), as a function of energy. (b) PDOS, projected onto Au $5d_{z2}$, 6s and $6p_z$ orbitals, as function of energy. (c) PDOS onto N 2s and $2p_z$ orbitals, and onto H 1s orbital. We identify σ bonding (hybridization between Au $5d_{z2}$, Au $6p_z$ and H 1s dominantly with some N s and p_z character) and σ^* antibonding (mainly Au 6s - H 1s - N p_z hybridization) orbitals, as well as a hybrid non-bonding (nb) orbital with Au 6s, Au d_{z2} and H 1s character. (d-e) Electron density difference $\Delta\rho$ between H-Au--(N)DCA and system composed of H-Au and isolated DCA (d), and between H-Au--(N)DCA and system composed of isolated neutral H and Au--DCA (e).

The electrostatic potentials in Figure S12c-d) show a partial positive charge δ^+ at the Au extremity of the H-Au system, and a partial negative charge δ^- at the DCA N atom. We claim that the formation of the σ, nb and σ^* orbitals due to H-Au hybridization reduces the electrostatic repulsion between the occupied Au 5d orbitals and lone electron-pair of the DCA N atom; this stabilizes the complex.
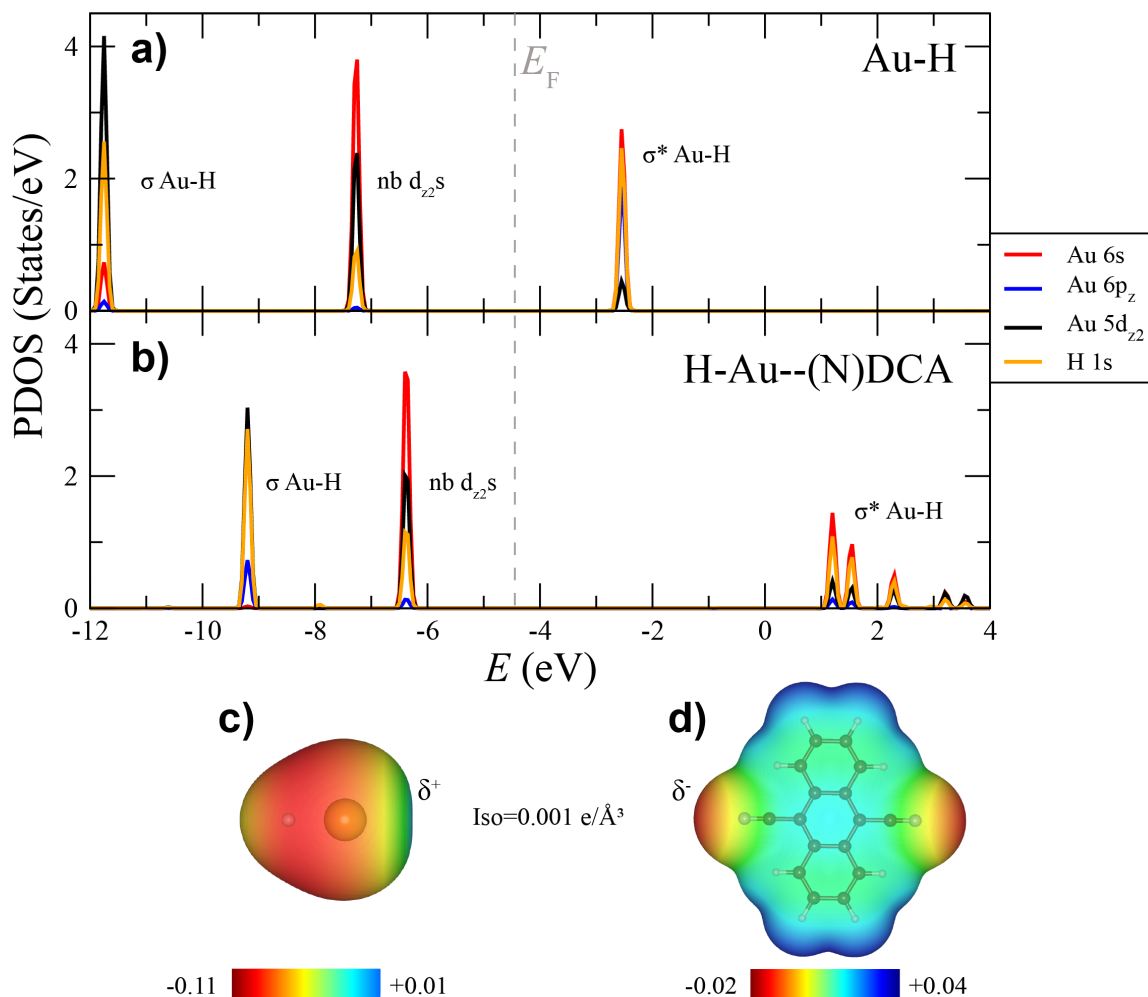

Figure S12: Comparison of PDOS of Au-H and H-Au--(N)DCA systems (projections onto Au $5d_{z^2}$, 6s and $6p_z$, and H 1s orbitals). (a) PDOS of Au-H system as a function of energy. (b) PDOS of H-Au--(N)DCA system as a function of energy. (c), (d) Isosurface (0.001 $e/$ Å^3) of electrostatic potential, Φ_{el} (calculated from the DFT electron density), for Au-H (c) and isolated DCA (d) systems, showing electrostatic attraction between Au and DCA N atom.

The hybridization between Au $5d_{z2}$, Au 6s and Au $6p_z$ orbitals in H-Au and H-Au---(N)DCA is similar to that observed in linear Au(I) complexes, where fully occupied Au 5d and empty 6s orbitals are nearly degenerate.[19] In these Au(I) complexes, $5d_{z2}$ and 6s orbitals hybridize as illustrated in Figure S13a). The $\Psi_1 = d_{z2} + s$ orbital is fully occupied and thus remains non-bonding (nb). Its torus shape lowers the electrostatic repulsion with nearby ligands (often facilitating linear Au complexes with a coordination number of 2). The $\Psi_2 = d_{z2} - s$ orbital is empty and can further hybridize with the Au $6p_z$ orbital, forming two hybrid Au 5d - Au 6s - Au 6p acceptor orbitals $\Psi_2 \pm p_z$ as shown in Figure S13b).

In the case of H-Au--(N)DCA above, we only observed hybridization between Au 5d and Au 6s orbitals. The resulting Ψ_1 orbital is non-bonding, while Ψ_2 forms a σ bond with H 1s. There is no indication of further hybridization with Au 6p orbitals nor of dative bonding between N and Au. After the formation of the covalent H-Au bond, the electron density related to the Ψ_2 orbital is similar to that of hydrogen, thus lowering its repulsion with the lone electron pair of nitrogen.
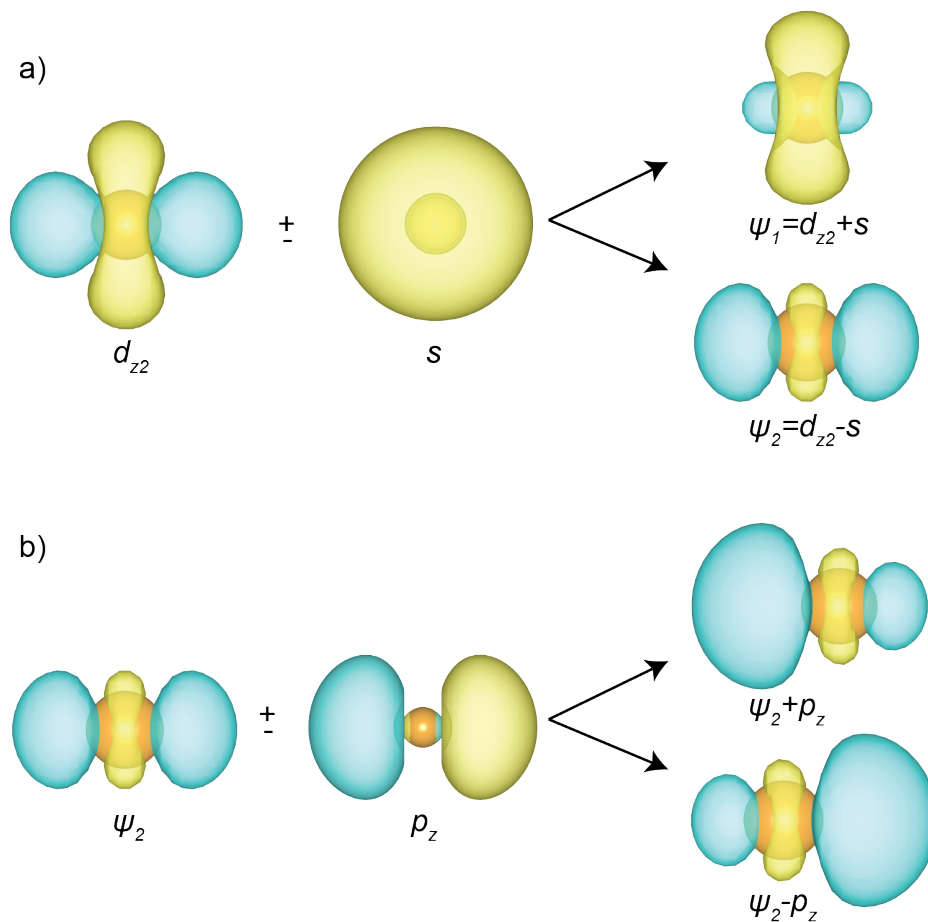
Figure S13: Hybridization of Au $5d_{z2}$, Au 6s and Au $6p_z$ states. (a) Schematic of Au $5d_{z2}$ - Au 6s hybridization, forming orbitals Ψ_1 and Ψ_2. Upon Au-H bonding, both these orbitals can hybridize with H 1s. Ψ_1 gives rise to the non-bonding orbital present in Figures S9-S12 whereas Ψ_2 gives rise to σ bonding and σ^* anti-bonding orbitals in H-Au and H-Au--(N)DCA. (b) Further hybridization between Ψ_2 and Au $6p_z$ orbital yields two equivalent linear orbitals $\Psi_2 \pm p_z$, as observed in coordination chemistry of Au(I).

We claim that when the system composed of 2 DCA molecules and a Au adatom on Ag(111) is in the initial state IS_{2A} [consisting of Au--(N)DCA and another DCA; see Figure 5c) in main text], a position A C-H stretching mode can facilitate the cleavage of the C-H bond closest to Au. We claim that the stabilization of the Au--N interaction as the system progressively transitions from Au--(N)DCA to H-Au--(N)DCA is at the basis of the low C-H activation barrier observed.

S10 Tentative pathway to organometallic dimers

Figure S14 highlights the geometry at the edge of a self-assembled DCA-only domain. The arrangement of DCA molecules at such an edge is similar to that in initial states IS_{2A} and IS_{2B} in Figure 5c), d) of main text (omitting Au atom).
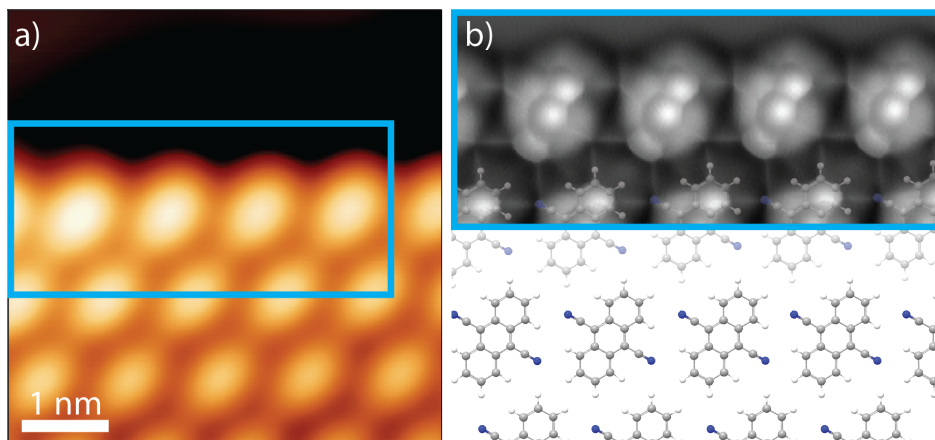

Figure S14: a) Constant-current STM image showing the edge of a self-assembled DCA-only domain on Ag(111) ($V_b = -50$ mV, $I_t = 50$ pA). b) NcAFM image acquired at the blue box in a) (acquired at a height 30 pm closer to the sample than the setpoint $V_b = 15$ mV, $I_t = 100$ pA) with overlaid ball-and-stick model of self-assembly . These images highlight the geometry at the edge of the DCA film.

We observed self-assembled DCA+Au domains composed of organometallic DCA-Au-DCA dimers both via co-deposition of Au and DCA, and via sequential deposition of DCA and then Au. This shows that the DCA-Au-DCA units can form after the DCA-only self-assembly. The supramolecular DCA-only domains are robust, with each DCA molecule within the domain participating in eight non-covalent H–N bonds with neighboring molecules, with each bond having an interaction energy of ~7.1 kcal/mol based on DFT calculations (B3LYP level). We suggest that the self-assembled DCA-only domains may facilitate the Au-induced C-H bond cleavage, with Au adatoms interacting with cyano groups at the edge of the DCA-only domains. In the following, we propose a tentative reaction pathway from self-assembled DCA-only domains to the observed organometallic DCA-Au-DCA units; see Figure S15. Figure S15a) shows an Au adatom interacting with a cyano N

atom of an edge DCA molecule, forming the initial state IS_{2A} of Figure 5c) in the main text. This then can lead to the cleavage of the position A C-H bond of an adjacent edge DCA molecule [Figure S15b)], resulting in an intermediate state similar to that of IM_{2A} [Figure 5c) of main text] with a DCA· radical. Based on DFT (GGA-PBE) calculations, we suggest that, subsequently, the hydrogen atom is likely to prefer bonding directly to Ag(111) than to the Au adatom on Ag(111) - as the former case is ∼4.5 kcal/mol more stable. This would allow the DCA· radical to then further react with a Au adatom [Figure S15c), d)], and finally with another DCA· radical, forming the organometallic DCA-Au-DCA dimer that we observed experimentally. We also suggest that non-covalent N–H bonds between neighboring DCA-Au-DCA within a DCA+Au domain contribute to the stabilization of this phase (which are not accounted for in simulations shown in Figure 5).
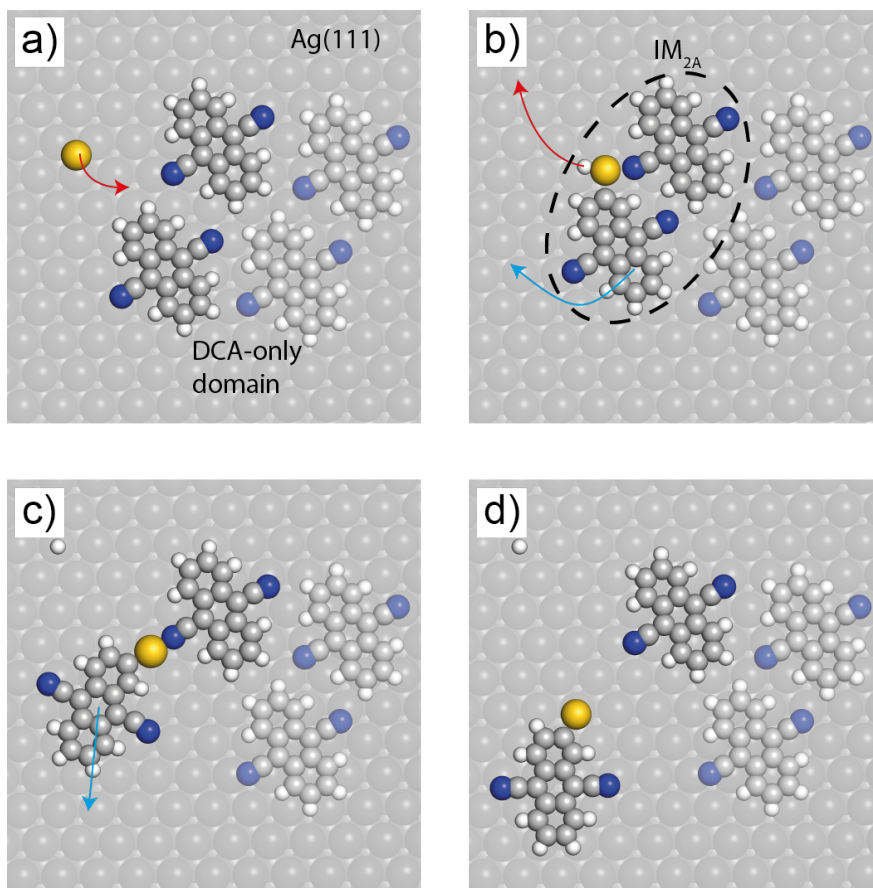
Figure S15: Ball-and-stick schematic of C-H bond cleavage mechanism at DCA-only domain edge. (a) Au adatom interacts with cyano N atom of DCA molecule at DCA-only domain edge, forming a Au--(N)DCA metal-organic complex and the initial state IS_{2A} [Figure 5c) of main text]. (b) Metal-organic Au--(N)DCA complex at DCA-only domain edge interacts with adjacent DCA molecule. This leads to cleavage of position A C-H bond in the adjacent DCA molecule, resulting in the formation of transition (TS_{2A}) and intermediate (IM_{2A}) states [Figure 5c) of main text] composed of a metal-organic H-Au--(N)DCA complex and a DCA· radical. Blue arrow represents rotation of DCA· radical to accommodate linear H-Au--(N)DCA complex in IM_{2A}. Red arrow illustrates subsequent migration of H atom from Au adatom onto Ag(111) surface. (c) Radical DCA· molecule can then interact with Au adatom and form a C-Au covalent bond. Blue arrow represents dissociation of Au--N bond and detachment of DCA(C)-Au complex from DCA-only domain. (d) DCA(C)-Au complex can then diffuse and interact with another DCA· radical, forming an organometallic DCA-Au-DCA unit.

S11   Second C-H bond activation

We considered the possibility of a second position A C-H bond cleavage occurring at the anthracene end opposite to Au in a DCA-Au-DCA dimer. Figure S16 shows transition states (TS) of a system composed of an organometallic DCA-Au-DCA unit, an extra DCA molecule and an extra Au adatom on Ag(111). We performed QM/MM calculations (at $T = 0$ K) of total energy differences ΔE (i.e., estimates of activation barriers) between TS and IS for C-H bond cleaving in a DCA-Au-DCA dimer, at position A opposite to the Au center, mediated by a metal-organic Au--(N)DCA complex [Figure S16a)]. We obtained $\Delta E_{\text{TS-IS}} \approx 63.0$ kcal/mol. This energy difference is $\sim$twice that estimated for a position A C-H bond cleavage in an isolated DCA, mediated by a Au--(N)DCA-Au-DCA complex [~ 31.8 kcal; Figure S16b)]. This suggests that the formation of 1D -[Au-DCA-Au-DCA]-organometallic chains is not energetically favorable, and that the DCA-Au-DCA dimers are stable discrete units, consistent with our experimental observations.
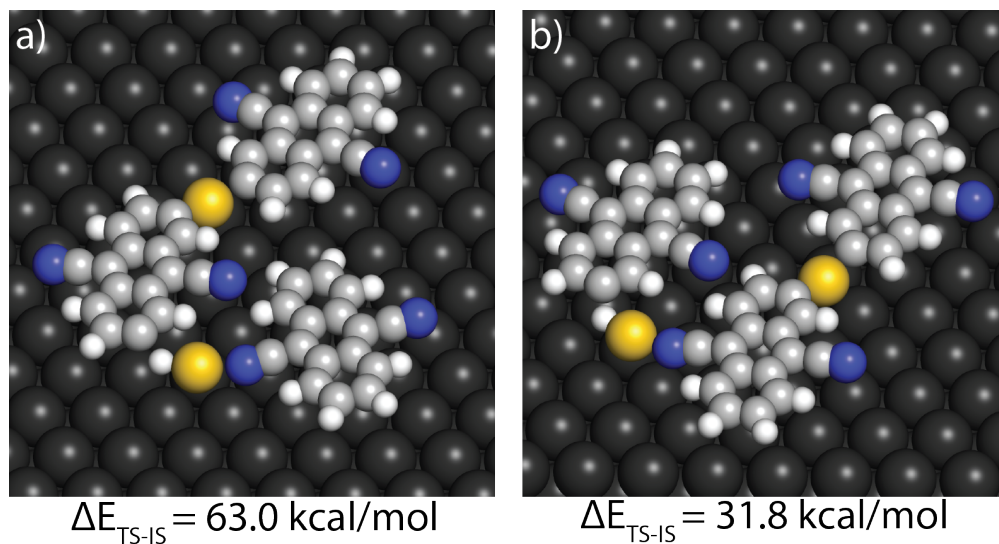
$\Delta E_{TS-IS} = 63.0$ kcal/mol $\Delta E_{TS-IS} = 31.8$ kcal/mol

Figure S16: QM/MM calculated total energy differences at $T = 0$ K, ΔE, between transition (TS) and initial (IS) states of systems comprised of an organometallic DCA-Au-DCA unit, an extra DCA molecule and an extra Au adatom on Ag(111). (a) Energy difference between TS and IS for cleavage of position A C-H bond in DCA-Au-DCA dimer opposite to Au center, mediated by Au--(N)DCA complex, is 63.0 kcal/mol. (b) Energy difference between TS and IS position A C-H bond cleavage in isolated DCA, mediated by Au–(N)DCA-Au-DCA complex, is significantly lower, 31.8 kcal/mol. This suggests that 1D -[Au-DCA-Au-DCA]- organometallic polymerization is not favorable, consistent with the experimental observation of discrete DCA-Au-DCA dimers.

References

(1) Frisch, M. J. et al. Gaussian16 Revision C.01. 2016.

(2) Chai, J.-D.; Head-Gordon, M. Long-range corrected hybrid density functionals with damped atom–atom dispersion corrections. *Phys. Chem. Chem. Phys.* **2008**, *10*, 6615–6620.

(3) Weigend, F.; Ahlrichs, R. Balanced basis sets of split valence, triple zeta valence and quadruple zeta valence quality for H to Rn: Design and assessment of accuracy. *Phys. Chem. Chem. Phys.* **2005**, *7*, 3297–3305.

(4) Blum, V.; Gehrke, R.; Hanke, F.; Havu, P.; Havu, V.; Ren, X.; Reuter, K.; Scheffler, M.

Ab initio molecular simulations with numeric atom-centered orbitals. *Computer Physics Communications* **2009**, *180*, 2175–2196.

(5) Lee, C.; Yang, W.; Parr, R. G. Development of the Colle-Salvetti correlation-energy formula into a functional of the electron density. *Phys. Rev. B* **1988**, *37*, 785–789.

(6) Tkatchenko, A.; Scheffler, M. Accurate Molecular Van Der Waals Interactions from Ground-State Electron Density and Free-Atom Reference Data. *Phys. Rev. Lett.* **2009**, *102*, 073005.

(7) Perdew, J. P.; Burke, K.; Ernzerhof, M. Generalized Gradient Approximation Made Simple. *Phys. Rev. Lett.* **1996**, *77*, 3865–3868.

(8) Case, D. A. et al. Amber 2020. 2020.

(9) Lewis, J. P.; Jelínek, P.; Ortega, J.; Demkov, A. A.; Trabada, D. G.; Haycock, B.; Wang, H.; Adams, G.; Tomfohr, J. K.; Abad, E.; Wang, H.; Drabold, D. A. Advances and applications in the FIREBALL ab initio tight-binding molecular-dynamics formalism. *physica status solidi (b)* **2011**, *248*, 1989–2007.

(10) Becke, A. D. Density-functional exchange-energy approximation with correct asymptotic behavior. *Phys. Rev. A* **1988**, *38*, 3098–3100.

(11) Grimme, S.; Ehrlich, S.; Goerigk, L. Effect of the damping function in dispersion corrected density functional theory. *Journal of Computational Chemistry* **2011**, *32*, 1456–1465.

(12) Basanta, M. A.; Dappe, Y. J.; Jelínek, P.; Ortega, J. Optimized atomic-like orbitals for first-principles tight-binding molecular dynamics. *Computational Materials Science* **2007**, *39*, 759–766.

(13) Becke, A. D. Density-functional thermochemistry. III. The role of exact exchange. *J. Chem. Phys.* **1993**, *98*, 5648–5652.

(14) Vosko, S. H.; Wilk, L.; Nusair, M. Accurate spin-dependent electron liquid correlation energies for local spin density calculations: a critical analysis. *Can. J. Phys.* **1980**, *58*, 1200–1211.

(15) Liu, X.; Matej, A.; Kratky, T.; Mendieta-Moreno, J. I.; Günther, S.; Mutombo, P.; Decurtins, S.; Aschauer, U.; Repp, J.; Jelinek, P.; Liu, S.-X.; Patera, L. L. Exploiting Cooperative Catalysis for the On-Surface Synthesis of Linear Heteroaromatic Polymers via Selective C–H Activation. *Angewandte Chemie International Edition* **2022**, *61*, e202112798.

(16) Hapala, P.; Kichin, G.; Wagner, C.; Tautz, F. S.; Temirov, R.; Jelínek, P. Mechanism of high-resolution STM/AFM imaging with functionalized tips. *Phys. Rev. B* **2014**, *90*, 085421.

(17) Kumar, D.; Krull, C.; Yin, Y.; Medhekar, N. V.; Schiffrin, A. Electric Field Control of Molecular Charge State in a Single-Component 2D Organic Nanoarray. *ACS Nano* **2019**, *13*, 11882–11890.

(18) Yan, L.; Pohjavirta, I.; Alldritt, B.; Liljeroth, P. On-Surface Assembly of Au-Dicyanoanthracene Coordination Structures on Au(111). *ChemPhysChem* **2019**, *20*, 2297–2300.

(19) Orgel, L. E. 843. Stereochemistry of metals of the B sub-groups. Part I. Ions with filled d-electron shells. *J. Chem. Soc.* **1958**, 4186–4190.

TOC Graphic
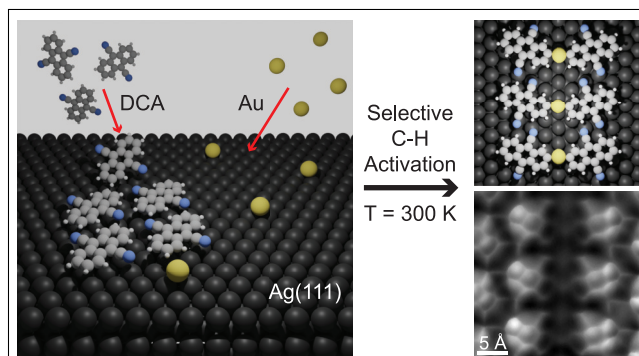
Deposition of Au atoms and 9,10-dicyanoanthracene (DCA) molecules on Ag(111) at room temperature (300 K) results in selective C-H activation to form organometallic DCA-Au-DCA dimers.